Comptes Rendus

Mécanique

Domenico Panunzio, Maria-Adela Puscas and Romain Lagrange

FSI—vibrations of immersed cylinders. Simulations with the engineering open-source code TrioCFD. Test cases and experimental comparisons

Short paper / *Note*

FSI—vibrations of immersed cylinders. Simulations with the engineering open-source code TrioCFD. Test cases and experimental comparisons

Domenico Panunzio[*, a]**, Maria-Adela Puscas**[b] **and Romain Lagrange**[*, a]

[a] Université Paris-Saclay, CEA, Service d'Etudes Mécaniques et Thermiques, 91191, Gif-sur-Yvette, France

[b] Université Paris-Saclay, CEA, Service de Thermohydraulique et de Mécanique des Fluides, 91191, Gif-sur-Yvette, France

E-mails: domenico.panunzio@cea.fr (D. Panunzio), maria-adela.puscas@cea.fr
(M.-A. Puscas), romain.lagrange@cea.fr, romain.g.lagrange@gmail.com (R. Lagrange)

Abstract. In this paper, we assess the capabilities of the Arbitrary Lagrangian–Eulerian (ALE) method implemented in the open-source code TrioCFD to tackle down two fluid–structure interaction problems involving moving boundaries. To test the code, we first consider the bi-dimensional case of two coaxial cylinders moving in a viscous fluid. We show that the two fluid forces acting on the cylinders are in phase opposition, with amplitude and phase that only depend on the Stokes number, the dimensionless separation distance and the Keulegan–Carpenter number. Throughout a detailed parametric study, we show that the self (resp. cross) added mass and damping coefficients decrease (resp. increase) with the Stokes number and the separation distance. Our numerical results are in perfect agreement with the theoretical predictions of the literature, thereby validating the robustness of the ALE method implemented in TrioCFD. Then, we challenge the code by considering the case of a vibrating cylinder located in the central position of a square tube bundle. In parallel to the numerical investigations, we also present a new experimental setup for the measurement of the added coefficient, using the direct method introduced by Tanaka. The numerical predictions for the self-added coefficients are shown to be in very good agreement with a theoretical estimation used as a reference by engineers. A good agreement with the experimental results is also obtained for moderate and large Stokes numbers, whereas an important deviation due to parasitic frequencies in the experimental setup appears for low Stokes number. Still, this study clearly confirms that the ALE method implemented in TrioCFD is particularly efficient in solving fluid–structure interaction problems. As an open-source code, and given its ease of use and its flexibility, we believe that TrioCFD is thus perfectly adapted to engineers who need simple numerical tools to tackle down complex industrial problems.

Keywords. Vibration, Fluid–structure interaction, Added mass, Added damping, Stokes number, ALE method, TrioCFD.

Manuscript received 30 September 2021, revised 21 July 2022 and 21 July 2022, accepted 22 July 2022.

---

* Corresponding authors.

1. Introduction

The accurate estimation of the force acting on a body moving in a viscous fluid is of crucial importance for engineers, particularly those working in fields such as turbomachinery [1], heat exchangers, tube banks [2,3] or energy harvesting of flexible structures [4–7]. When an immersed body is subjected to a small amplitude of motion, Stokes [8] showed that the fluid force is the sum of two terms: an added mass term related to the body's acceleration and a damping term related to the body's velocity. The concept of added mass and damping terms can be generalized to multiple immersed bodies, introducing some self and cross-added coefficients. In such a case, the self-added coefficients relate the fluid force on a body to its motion. On their hand, the cross-added coefficients relate the forces on a body to the other bodies' motion. The determination of the added coefficients has been the topic of considerable experimental, [9–14] and theoretical studies, mostly based on a Helmholtz decomposition associated with a method of images [15–20] or a conformal transformation [21–28]. These theoretical approaches have shown their efficiency in predicting the added-coefficients in some simple configurations, but extending to the industrial context remains delicate. As a consequence, engineers developed fast and robust numerical approaches, such as the immersed body method [29], the cut-cell method [30] or the penalization method [27,31–35].

In the present work, we aim to analysis the efficiency of the Arbitrary Lagrangian–Eulerian (ALE) method [36–38] implemented in the open-source code TrioCFD [39, 40], developed by the CEA for the nuclear industry. TrioCFD is a C++ object-oriented parallel software designed for calculations of unsteady laminar or turbulent fluid flows. The calculations are performed on structured (parallelepipeds) and non-structured (tetrahedrons) meshes of several millions of control volumes (hybrid finite volume element, see [39–41]). The code structure is flexible, allowing the user to choose the discretization method, the convection and time schemes, as well as the turbulence model.

This article is organized as follows. Section 2 presents the ALE method and the main equations solved by TrioCFD. In Section 3, we test the code, considering the vibration of two coaxial cylinders separated by a fluid layer. The added coefficients are extracted from the numerical predictions of the fluid forces, and the results are compared with those of the literature. In Section 4, we challenge the code, considering the vibration of a cylindrical tube located in the central position of a square tube array. Our numerical results for the fluid coefficients are compared with a phenomenological estimation used by engineers of the nuclear industry and with some experimental measurements that we have performed on a new experimental set-up built at CEA. Finally, Section 5 summarizes our findings.

2. Numerics

The numerical simulations of the Navier–Stokes equations have been conducted on the 1.8.0 version of TrioCFD, a programmable CFD code based on the TRUST platform and a C++ language architecture, see [39, 40]. This open source code allows the user to choose a wide range of options and parameters, among which the discretization schemes in space and time, the turbulence models (RANS or LES approaches) or the boundary conditions. Given its flexibility, the code is widely used in the nuclear industry for massive parallel and high performance calculations.

To determine the flow of a fluid, it is necessary to describe the kinematics of all its material particles throughout time. To do so, one can adopt either an Euler description of motion, in which a fluid particle is identified by its instantaneous position, or a Lagrange description of motion, in which a fluid particle is identified by its initial position. Both descriptions are totally equivalent, leading to different forms of the Navier–Stokes equations that can be discretized on a stationary mesh grid (Euler) or a mesh grid that follows the motion of the fluid particles (Lagrange).

In both cases, the mesh grids do not account for the motion of the boundaries, which makes the numerical simulations of the related Navier–Stokes equations delicate.

To overcome this problem, several approaches, such as the immersed boundary methods [42–44], or the ALE method [36–38] have been developed.

In the ALE approach, a fluid particle is identified by its position relative to a frame moving with a nonuniform velocity $\mathbf{v}_{\text{ALE}}$. In this new frame of reference, the Navier–Stokes equations are expressed as

$$\begin{cases} \nabla \cdot \mathbf{v} = 0, & \text{(a)} \\ \dfrac{\partial J\mathbf{v}}{\partial t} = J\left(\nu\Delta\mathbf{v} - \nabla \cdot ((\mathbf{v} - \mathbf{v}_{\text{ALE}}) \otimes \mathbf{v}) - \dfrac{1}{\rho}\nabla p\right), & \text{(b)} \end{cases} \tag{1}$$

with J the Jacobian of the transformation between the ALE and the Lagrange descriptions. The ALE method is actually a hybrid description between the Euler and the Lagrange descriptions, both of them corresponding to the particular cases $\mathbf{v}_{\text{ALE}} = \mathbf{0}$ and $\mathbf{v}_{\text{ALE}} = \mathbf{v}$, respectively. In the ALE framework, the choice of $\mathbf{v}_{\text{ALE}}$ is arbitrary as long as the deformation of the mesh grid remains under control. For moderate deformations, $\mathbf{v}_{\text{ALE}}$ is usually defined as the solution of an auxiliary Laplace problem, see [45].

In case of unstructured meshes (triangles in 2D or tetrahedrons in 3D), TrioCFD uses Finite Volume-Element (FVE) approach to solving discretized Navier–Stokes equations. These methods combine the finite element method with the finite volume method, gathering the advantages of each approach for incompressible Navier–Stokes problems [40, 41].

Applying the numerical FVE discretization on (1), along with the Forward Euler scheme for the time discretization, results in the following discrete system:

$$\begin{cases} [M]\dfrac{J^{n+1}\mathbf{V}_h^{n+1} - J^n\mathbf{V}_h^n}{\Delta t} = J^{n+1}\left([A]\mathbf{V}_h^{n+1} - [L(\mathbf{V}_h^n)]\mathbf{V}_h^{n+1} + [L(\mathbf{V}^n)]\mathbf{V}_{h,\text{ALE}}^{n+1} - [G]\mathbf{P}_h^{n+1}\right), & \text{(a)} \\ [D]\mathbf{V}_h^{n+1} = \mathbf{0}, & \text{(b)} \end{cases} \tag{2}$$

where $\mathbf{V}_h$ and $\mathbf{P}_h$ are the unknowns vectors of the discrete fluid flow velocity vector and pressure, Δt is the time step, $[M]$ is the mass matrix operator, $[A]$ is the discrete diffusion operator, $[L(\mathbf{V}_h)]$ is the non-linear discrete convection operator, $[G]$ is the discrete gradient operator, and $[D]$ is the discrete divergence operator. The superscripts n and $n+1$ indicate the time step at which the variable is computed.

In order to solve the velocity–pressure coupling, a multi-step (projection–correction) technique [46, 47] is employed, where an intermediate (predicted) velocity $\mathbf{V}_h^*$ is computed:

$$J^{n+1}\left(\frac{1}{\Delta t}[M] - [A] + [L(\mathbf{V}_h^n)]\right)\mathbf{V}_h^* = \frac{1}{\Delta t}[M]J^n\mathbf{V}_h^n + J^{n+1}[L(\mathbf{V}_h^n)]\mathbf{V}_{h,\text{ALE}}^n - J^{n+1}[G]\mathbf{P}_h^n, \tag{3}$$

and the mass conservation is then enforced by solving a Poisson equation for pressure:

$$[D][M]^{-1}[G]\mathbf{P}_h' = \frac{1}{\Delta t}[D]\mathbf{V}_h^*. \tag{4}$$

Finally, the velocity is updated using the predicted velocity $\mathbf{V}_h^*$ and the pressure increment $\mathbf{P}_h'$:

$$\mathbf{V}_h^{n+1} = \mathbf{V}_h^* - \Delta t[M]^{-1}[G]\mathbf{P}_h', \quad \mathbf{P}_h^{n+1} = \mathbf{P}_h^n + \mathbf{P}_h'. \tag{5}$$

In the present work, the linear systems (3) is solved by the iterative solver GMRES from the PETSc library [48].

3. Study 1. Vibrations of two coaxial cylinders in a viscous fluid

In this section, we test the capabilities of the code TrioCFD along with the ALE approach, considering the 2D case of two coaxial cylinders vibrating in a viscous fluid. The goal of this preliminary work is to introduce all the important concepts that will be used in the study of the
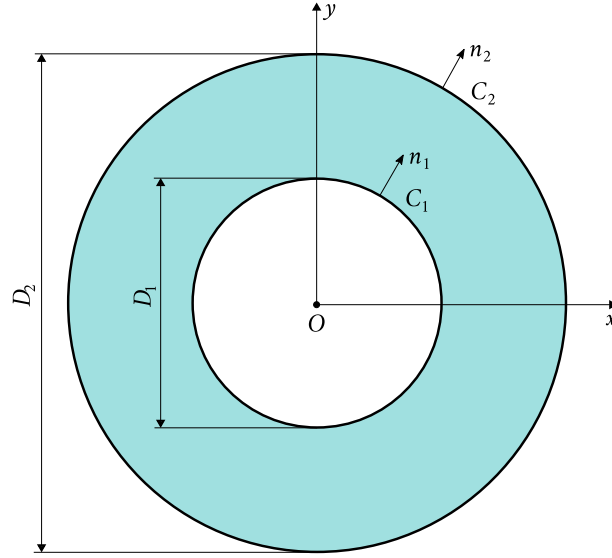
Figure 1. Configuration with two concentric cylinders. The fluid in the annulus region is homogeneous with mass density ρ and kinematic viscosity ν.

vibrations of a tube in a square bundle, considered in Section 4. In what follows, we introduce the problem, present the numerical setup and finally discuss our numerical results in comparison with the theoretical estimations of [49, 50].

3.1. *Presentation of the problem and governing equations*

Let C_1 and C_2 be two concentric cylinders with diameters D_j and boundaries ∂C_j, $j = \{1, 2\}$, see Figure 1. One cylinder, either C_1 or C_2, oscillates in the (x, y) plane with a simple harmonic motion of angular frequency Ω and a displacement amplitude U. The fluid in the annulus region is Newtonian, homogeneous, with mass density ρ and kinematic viscosity ν. The fluid flow generated by the oscillation of one cylinder is assumed as incompressible and two-dimensional.

The Navier–Stokes equations and the boundary conditions for the fluid flow $(\mathbf{v}, p)$ are:

$$
\begin{cases}
\nabla \cdot \mathbf{v} = 0, & \text{(a)} \\
\dfrac{\partial \mathbf{v}}{\partial t} + (\mathbf{v} \cdot \nabla)\mathbf{v} + \dfrac{1}{\rho}\nabla p - \nu \Delta \mathbf{v} = \mathbf{0}, & \text{(b)} \\
\mathbf{v} - \dfrac{\mathrm{d}\mathbf{U}}{\mathrm{d}t} = \mathbf{0} \quad \text{on } \partial C_j, j = \{1, 2\}. & \text{(c)}
\end{cases}
\tag{6}
$$

The (6c) ensures the continuity of velocities at the cylinder boundaries ∂C_j. The fluid force acting on C_j is the sum of a pressure and a viscous term

$$
\mathbf{F}_j = -\int_{\partial C_j} p\mathbf{n}_j \, \mathrm{d}L_j + \rho\nu \int_{\partial C_j} [\nabla \mathbf{v} + (\nabla \mathbf{v})^{\mathrm{T}}] \cdot \mathbf{n}_j \, \mathrm{d}L_j,
\tag{7}
$$

where $\mathbf{n}_j$ is the outward normal unit vector to ∂C_j, see Figure 1, and $\mathrm{d}L_j$ is an infinitesimal line element of integration.

Picking $D_1/2$ and Ω^{-1} as a characteristic length and time, the dimensionless quantities t^*, $\mathbf{u}^*$, $\mathbf{v}^*$, p^* and $\mathbf{f}_j^*$ are defined as

$$
t = \Omega^{-1}t^*, \quad \mathbf{U} = U\mathbf{u}^*, \quad \mathbf{v} = U\Omega\mathbf{v}^*, \quad p = \rho U \frac{D_1}{2}\Omega^2 p^*, \quad \mathbf{F}_j = \rho U \left(\frac{D_1}{2}\Omega\right)^2 \mathbf{f}_j^*.
\tag{8}
$$

To reduce the number of parameters of the problem, the following rescaled quantities are also defined

$$\varepsilon = \frac{D_2}{D_1}, \quad KC = \frac{U}{D_1}, \quad Sk = \frac{D_1^2(\Omega/2\pi)}{\nu},$$
(9)

as the dimensionless separation distance, the Keulegan–Carpenter number and the Stokes number, respectively. Introducing (8) in (6) yields the dimensionless Navier–Stokes equations

$$\begin{cases} \nabla \cdot \mathbf{v}^* = 0, & \text{(a)} \\ \dfrac{\partial \mathbf{v}^*}{\partial t^*} + 2KC(\mathbf{v}^* \cdot \nabla)\mathbf{v}^* + \nabla p^* - \dfrac{2}{\pi Sk}\Delta \mathbf{v}^* = \mathbf{0}, & \text{(b)} \\ \mathbf{v}^* - \dfrac{\mathrm{d}\mathbf{u}^*}{\mathrm{d}t^*} = \mathbf{0} \quad \text{on } \partial C_j, j = \{1, 2\}. & \text{(c)} \end{cases}$$
(10)

The dimensionless fluid force acting on C_j is

$$\mathbf{f}_j^* = -\int_{\partial C_j} p^* \mathbf{n}_j \, \mathrm{d}l_j + \frac{2}{\pi Sk} \int_{\partial C_j} [\nabla \mathbf{v}^* + (\nabla \mathbf{v}^*)^{\mathrm{T}}] \cdot \mathbf{n}_j \, \mathrm{d}l_j,$$
(11)

with $\mathrm{d}l_j = 2\,\mathrm{d}L_j/D_1$.

For $KC \ll 1$, the dimensionless Navier–Stokes equations are linear. It follows that the fluid forces are linear combinations of the cylinder velocity $\mathrm{d}\mathbf{u}^*/\mathrm{d}t^*$ and acceleration $\mathrm{d}^2\mathbf{u}^*/\mathrm{d}t^{*2}$

$$\mathbf{f}_j^* = -\pi \left([M_j]\frac{\mathrm{d}^2\mathbf{u}^*}{\mathrm{d}t^{*2}} + [C_j]\frac{\mathrm{d}\mathbf{u}^*}{\mathrm{d}t^*} \right),$$
(12)

with

$$[M_j] = \begin{pmatrix} m_{\mathrm{self}}^{(j)} \\ & m_{\mathrm{self}}^{(j)} \end{pmatrix} \quad \text{and} \quad [C_j] = \begin{pmatrix} c_{\mathrm{self}}^{(j)} \\ & c_{\mathrm{self}}^{(j)} \end{pmatrix} \quad \text{if } C_j \text{ is moving,}$$
(13a)

$$[M_j] = \begin{pmatrix} m_{\mathrm{cross}} \\ -m_{\mathrm{cross}} \end{pmatrix} \quad \text{and} \quad [C_j] = \begin{pmatrix} c_{\mathrm{cross}} \\ -c_{\mathrm{cross}} \end{pmatrix} \quad \text{if } C_j \text{ is stationary.}$$
(13b)

The self-added mass and damping coefficients $m_{\mathrm{self}}^{(j)}$ and $c_{\mathrm{self}}^{(j)}$ relate the fluid force on the moving cylinder to its own motion. The cross-added mass and damping coefficients m_{cross} and c_{cross} relate the fluid force on the stationary cylinder to the motion of the other cylinder. The fluid added coefficients are functions of the dimensionless separation distance ε and the Stokes number Sk.

For a harmonic displacement $\mathbf{u}^* = \sin(t^*)\mathbf{e}_x$, the dimensionless fluid forces (12) reduce to

$$\mathbf{f}_j^* = \pi \left(m_{\mathrm{self}}^{(j)} \sin(t^*) - c_{\mathrm{self}}^{(j)} \cos(t^*) \right) \mathbf{e}_x, \quad \text{if } C_j \text{ is moving,}$$
(14a)

$$\mathbf{f}_j^* = \pi (m_{\mathrm{cross}} \sin(t^*) - c_{\mathrm{cross}} \cos(t^*)) \mathbf{e}_x, \quad \text{if } C_j \text{ is stationary,}$$
(14b)

or similarly $\mathbf{f}_j^* = h_j \sin(t^* + \varphi_j)\mathbf{e}_x$, with

$$h_j = \pi\sqrt{\left(m_{\mathrm{self}}^{(j)}\right)^2 + \left(c_{\mathrm{self}}^{(j)}\right)^2} \quad \text{and} \quad \varphi_j = -\arctan\left(\frac{c_{\mathrm{self}}^{(j)}}{m_{\mathrm{self}}^{(j)}}\right) \quad \text{if } C_j \text{ is moving,}$$
(15a)

$$h_j = \pi\sqrt{m_{\mathrm{cross}}^2 + c_{\mathrm{cross}}^2} \quad \text{and} \quad \varphi_j = \pi - \arctan\left(\frac{c_{\mathrm{cross}}}{m_{\mathrm{cross}}}\right) \quad \text{if } C_j \text{ is stationary.}$$
(15b)

Yeh *et al.* [50] derived a few analytical expressions of the fluid added coefficients. Introducing $\Re$ and $\Im$ the real and imaginary part operators, these expressions are as follows

$$m_{\mathrm{self}}^{(1)} = \Re(a_{11}), \quad m_{\mathrm{self}}^{(2)} = \varepsilon^2 \Re(a_{22}), \quad m_{\mathrm{cross}} = \varepsilon \Re(a_{12}),$$
(16a)

$$c_{\mathrm{self}}^{(1)} = \Im(-a_{11}), \quad c_{\mathrm{self}}^{(2)} = \varepsilon^2 \Im(-a_{22}), \quad c_{\mathrm{cross}} = \varepsilon \Im(-a_{12}),$$
(16b)

with $a_{11} = -(1 + 2a)$, $a_{22} = 2a/\varepsilon$, $a_{12} = 1 - 2a/\varepsilon^2$ and

$$a = \begin{vmatrix} 1 & 1 & J_1(\beta_1) & Y_1(\beta_1) \\ 0 & 1 & \varepsilon^{-1}J_1(\beta_2) & \varepsilon^{-1}Y_1(\beta_2) \\ 2 & 2 & \beta_1 J_0(\beta_1) & \beta_1 Y_0(\beta_1) \\ 0 & 2 & \beta_1 J_0(\beta_2) & \beta_1 Y_0(\beta_2) \end{vmatrix} \begin{vmatrix} 1 & 1 & J_1(\beta_1) & Y_1(\beta_1) \\ \varepsilon^{-2} & 1 & \varepsilon^{-1}J_1(\beta_2) & \varepsilon^{-1}Y_1(\beta_2) \\ 0 & 2 & \beta_1 J_0(\beta_1) & \beta_1 Y_0(\beta_1) \\ 0 & 2 & \beta_1 J_0(\beta_2) & \beta_1 Y_0(\beta_2) \end{vmatrix}^{-1}. \tag{17}$$

In (17), J_n and Y_n are the Bessel functions of the first and second kind, with arguments $\beta_1 = (1 - i)\sqrt{\pi}/2\sqrt{Sk}$ or $\beta_2 = \varepsilon\beta_1$.

From an asymptotic expansion of these functions as $Sk \to \infty$, we show that $(m_{\text{self}}^{(j)}, m_{\text{cross}}, c_{\text{self}}^{(j)}, c_{\text{cross}})$ are equivalent to $(\widetilde{m}_{\text{self}}^{(j)}, \widetilde{m}_{\text{cross}}, \widetilde{c}_{\text{self}}^{(j)}, \widetilde{c}_{\text{cross}})$ with

$$\widetilde{m}_{\text{self}}^{(j)} = m_{\text{self}}^{(j)\text{pot}} + \frac{4}{\sqrt{\pi}}\frac{1}{\sqrt{Sk}}, \quad \widetilde{m}_{\text{cross}} = m_{\text{cross}}^{\text{pot}} - \frac{4}{\sqrt{\pi}}\frac{1}{\sqrt{Sk}}, \tag{18a}$$

$$\widetilde{c}_{\text{self}}^{(j)} = \frac{4}{\sqrt{\pi}}\frac{1}{\sqrt{Sk}}\frac{\varepsilon^4 + \varepsilon}{(\varepsilon^2 - 1)^2}, \quad \widetilde{c}_{\text{cross}} = -\frac{4}{\sqrt{\pi}}\frac{1}{\sqrt{Sk}}\frac{\varepsilon^4 + \varepsilon}{(\varepsilon^2 - 1)^2}, \tag{18b}$$

and

$$m_{\text{self}}^{(1)\text{pot}} = \frac{\varepsilon^2 + 1}{\varepsilon^2 - 1}, \quad m_{\text{self}}^{(2)\text{pot}} = \frac{\varepsilon^2(\varepsilon^2 + 1)}{\varepsilon^2 - 1}, \quad m_{\text{cross}}^{\text{pot}} = -\frac{2\varepsilon^2}{\varepsilon^2 - 1}. \tag{19}$$

The terms $m_{\text{self}}^{(j)\text{pot}}$ and $m_{\text{cross}}^{\text{pot}}$ are the inviscid limits of $m_{\text{self}}^{(j)}$ and m_{cross} as $Sk \to \infty$. These terms can also be obtained from a potential theory in which the fluid forces are only due to the pressure field. Note that $c_{\text{self}}^{(j)\text{pot}} = c_{\text{cross}}^{\text{pot}} = 0$ as there are not damping effects in the inviscid framework.

In Section 3.3 the theoretical estimations (16) and (18) are compared with the numerical predictions performed with TrioCFD. Numerically, the fluid forces acting on ∂C_j are computed by the sum of the pressure and viscous terms in (7) given by TrioCFD. To extract the added coefficients from the numerical simulations of the dimensionless fluid forces, we introduce the Fourier inner product over five periods

$$\langle f(t^*), g(t^*) \rangle = \frac{1}{5\pi}\int_0^{10\pi} f(t^*)g(t^*)\,\mathrm{d}t^*. \tag{20}$$

From (14), it follows that the added-coefficients are

$$m_{\text{self}}^{(j)} = \frac{\langle \sin(t^*), \mathbf{f}_j^*(t^*) \cdot \mathbf{e}_x \rangle}{\pi} \quad \text{and} \quad c_{\text{self}}^{(j)} = -\frac{\langle \cos(t^*), \mathbf{f}_j^*(t^*) \cdot \mathbf{e}_x \rangle}{\pi} \quad \text{if } C_j \text{ is moving}, \tag{21a}$$

$$m_{\text{cross}} = \frac{\langle \sin(t^*), \mathbf{f}_j^*(t^*) \cdot \mathbf{e}_x \rangle}{\pi} \quad \text{and} \quad c_{\text{cross}} = -\frac{\langle \cos(t^*), \mathbf{f}_j^*(t^*) \cdot \mathbf{e}_x \rangle}{\pi} \quad \text{if } C_j \text{ is stationary}. \tag{21b}$$

3.2. *Numerical setup*

To discretize the fluid domain, we use an unstructured grid of triangles generated by the Gmsh platform, see [51]. Due to its adaptive and automatic algorithm, Gmsh makes it possible to choose between two different local sizes for the 2D mesh: a small local size, lc_{fine}, for elements close to the moving cylinder and a large local size, lc, for elements close to the stationary cylinder. In this way, a refined mesh is used in the regions with large gradient fields whereas a loose mesh is used in the areas with low gradient fields. In Appendix B, a mesh sensitivity analysis clearly shows a convergence of the mass coefficients as lc and lc_{fine} are changed. The convergence of the damping coefficients is less obvious, especially for high values of Sk. Physically, this is related to the thickness of the boundary layer, which tends to zero as Sk increases. It follows that a finer mesh is required close to a cylinder boundary to account for the thickness of the boundary layer
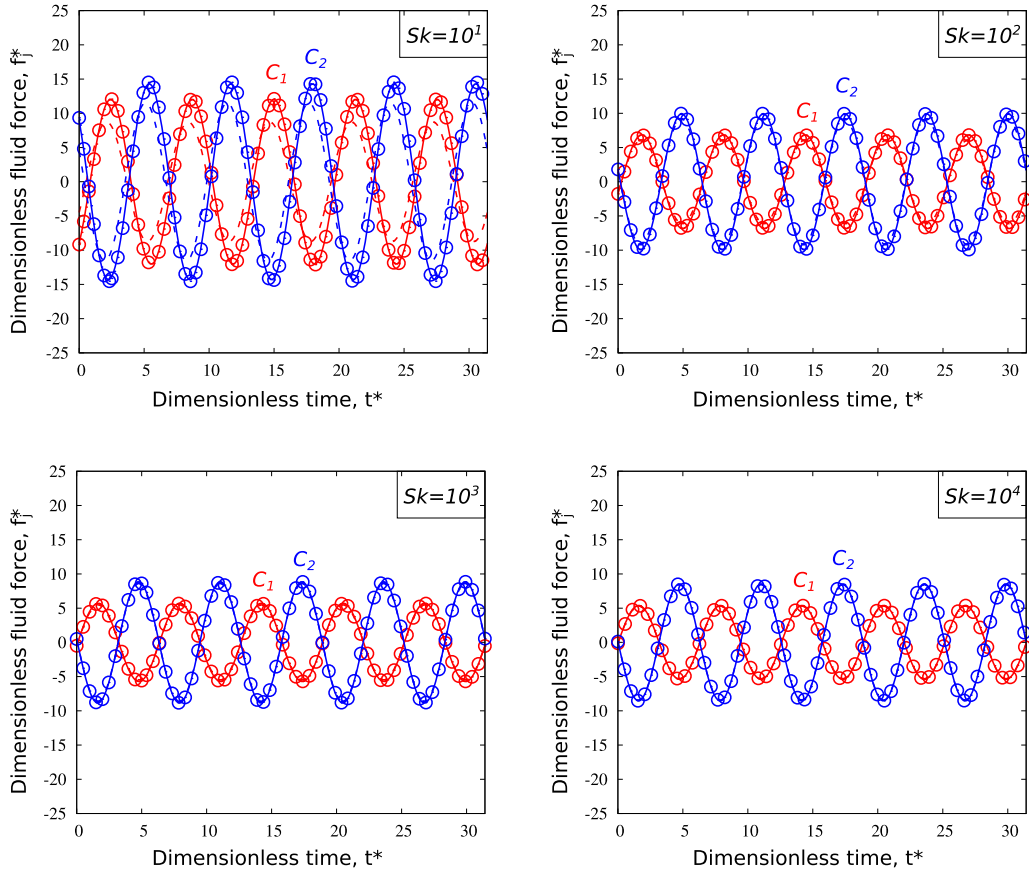
Figure 2. Study 1. Time evolution of the dimensionless fluid forces, for $Sk = \{10^1, 10^2, 10^3, 10^4\}$, $\varepsilon = 2$ and $KC = 10^{-2}$. The red and blue solid lines correspond to the theoretical estimations of [50], see (16). The dashed lines (indistinguishable from the solid lines for $Sk > 10^2$) correspond to the theoretical asymptotic expansion $Sk \to \infty$, see (18). The symbols correspond to the numerical predictions.

and obtain an accurate estimation of the damping terms. In this work, a compromise between the time of calculation and the precision (throughout of this work, we indicate the relative deviations of our numerical results compared to other theoretical or experimental references) is made to choose adequate values for lc and lc_{fine}.

3.3. *Results and discussion*

The inner cylinder is imposed a sinusoidal displacement in the x-direction for five time periods, i.e. $\mathbf{u}^* = \sin(t^*)\mathbf{e}_x$ with $t^* \in \{0, 10\pi\}$. The numerical simulations are performed for $\varepsilon \in \{1.25, 1.5, 2\}$, $Sk \in \{10^1, 10^2, 10^3, 10^4\}$ and $KC = 10^{-2}$.

The time evolution of the dimensionless fluid forces is represented in Figures 2 and 3. A perfect agreement is obtained between theoretical estimations and numerical predictions. The fluid forces are sinusoidal functions in phase opposition. In Figures 4 and 5, we show that the amplitudes h_j (resp. phases φ_j) decrease (resp. increase) with both Sk and ε, recovering the asymptotic limits as $Sk \to \infty$ (inviscid limit) and as $\varepsilon \to \infty$ (isolated cylinder limit).
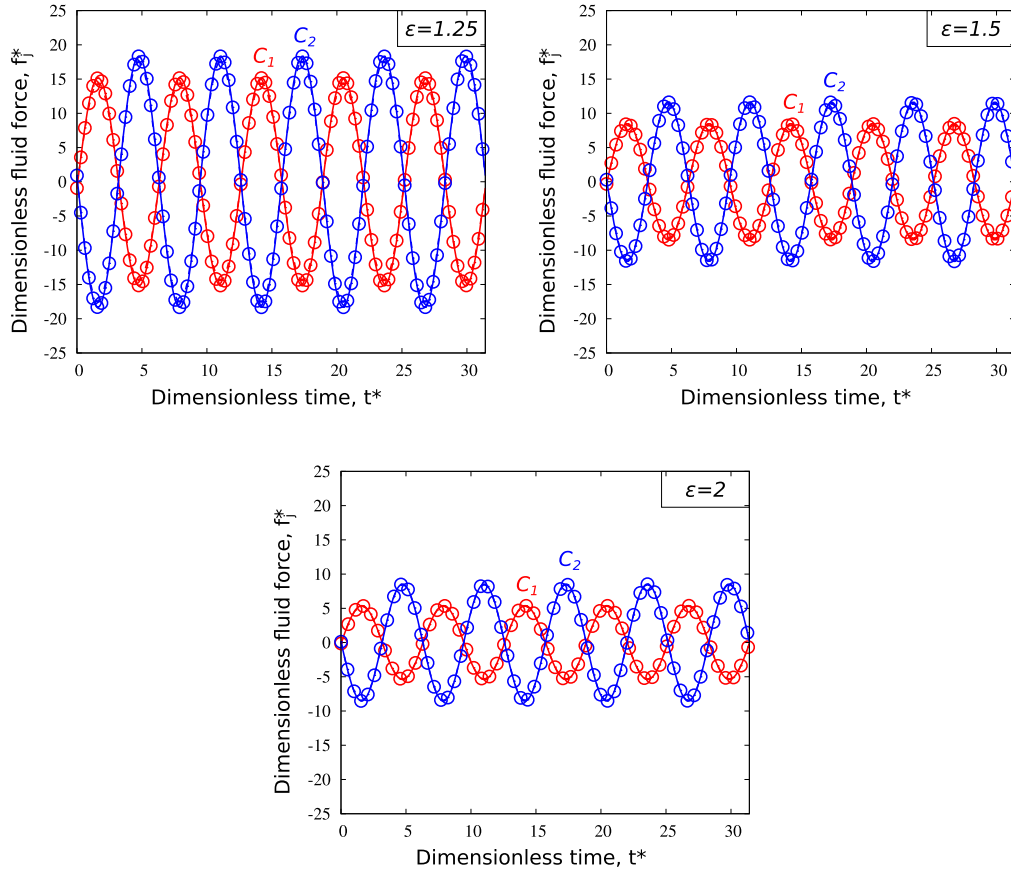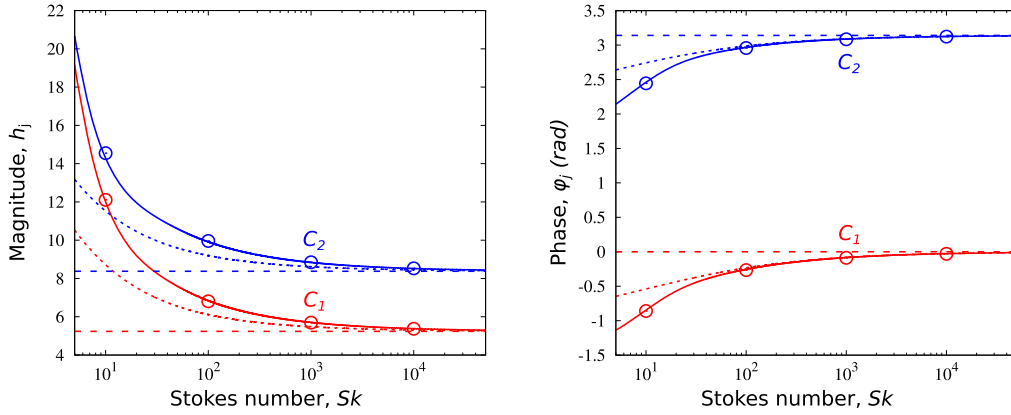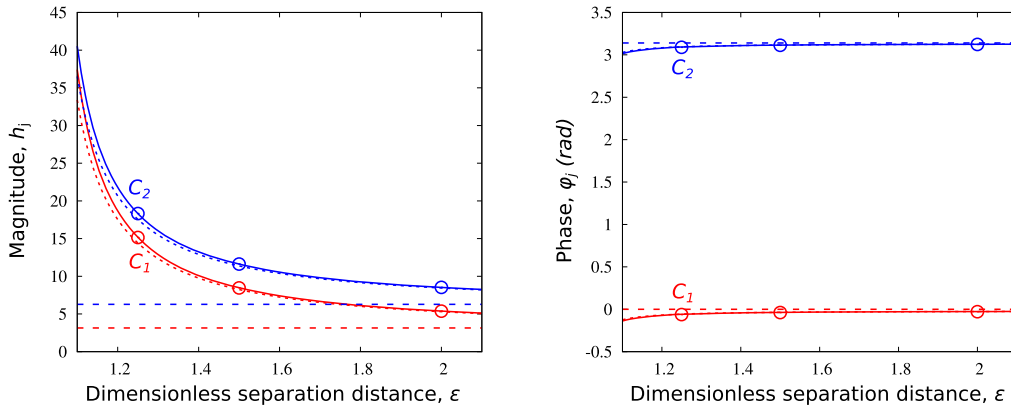
Figure 3. Study 1. Time evolution of the dimensionless fluid forces, for $\varepsilon = \{1.25, 1.5, 2\}$, $Sk = 10^4$ and $KC = 10^{-2}$. The red and blue solid lines correspond to the theoretical estimations of [50], see (16). The symbols correspond to the numerical predictions.

The evolution of the added coefficients is depicted in Figures 6 and 7. The numerical predictions are in very good agreement with the theoretical estimations, even if a tiny difference is observed in the range of low Stokes numbers in which the theoretical estimations reach their limit of validity. Still, we confirm that the self (resp. cross) added coefficients decrease (resp. increase) with both Sk and ε, recovering the asymptotic limits as $Sk \to \infty$ (inviscid limit) and as $\varepsilon \to \infty$ (isolated cylinder limit).

We introduce the quantity ι, defined as the relative deviation between the numerical and the exact theoretical predictions [50] of some quantity Q: $\iota = |Q_{\text{th}} - Q_{\text{num}}|/|Q_{\text{th}}|$. Figure 8 and Tables A1, A2 in Appendix A show that ι is very low for the added mass coefficients and it becomes greater for the added damping coefficients as Sk increases but seems to be weakly influenced by ε. In fact, for large values of Sk, the damping coefficients become very small and even small differences from the theoretical value produce significant deviations. Physically, this is related to the thickness of the boundary layer, which tends to zero: to reduce ι for the damping coefficients a finer mesh at the cylinder boundaries would be required. We shall note that the theoretical approach [49, 50] is fully linear since the convective term $2KC(\mathbf{v}^* \cdot \nabla)\mathbf{v}^*$ of the Navier–Stokes equation (10b) is neglected. In the numerical simulations, the nonlinear convective term is retained through a small but nonzero Keulegan–Carpenter number $KC = 10^{-2}$. However, this
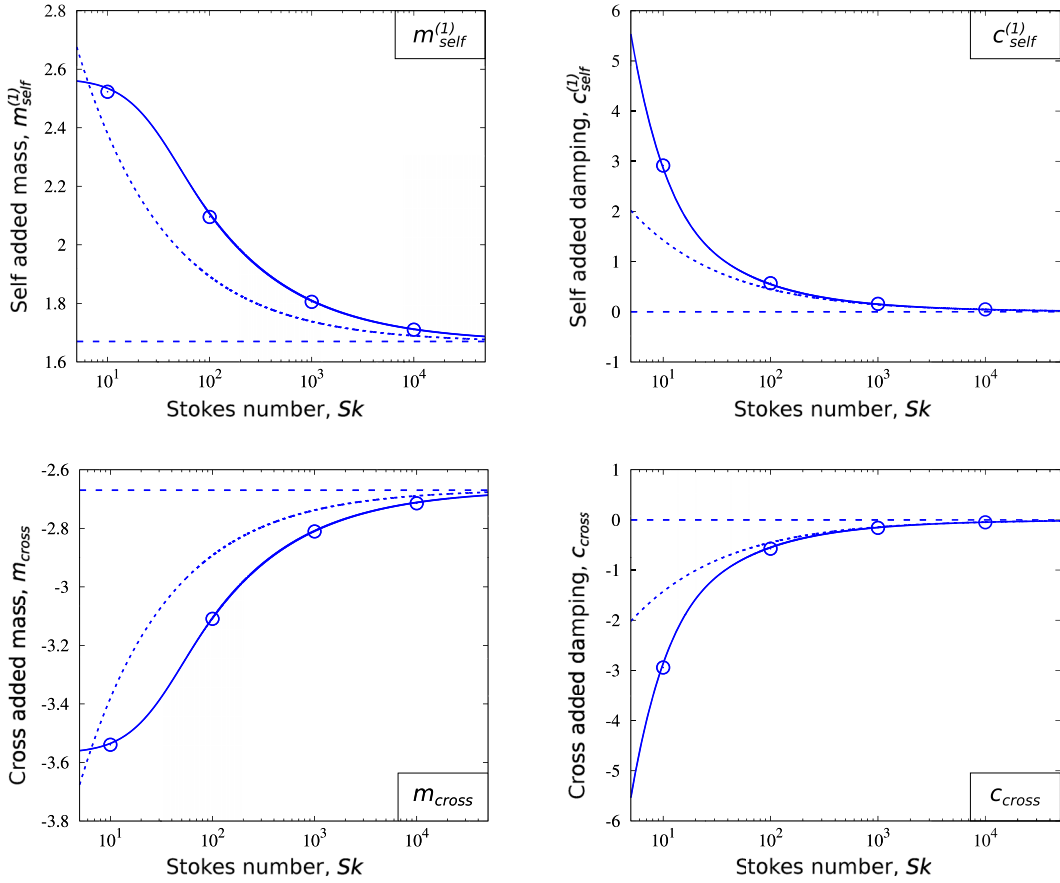
Figure 4. Study 1. Evolution of the magnitudes h_j and phases φ_j with the Stokes number Sk, for $\varepsilon = 2$ and $KC = 10^{-2}$. The red and blue solid lines correspond to the theoretical estimations of [50], see (16). The dashed lines correspond to the theoretical asymptotic expansion $Sk \to \infty$, see (18). The horizontal dashed lines correspond to the theoretical inviscid limits as $Sk \to \infty$. The symbols correspond to the numerical predictions.

Figure 5. Study 1. Evolution of the magnitudes h_j and phases φ_j with the dimensionless separation distance ε, for $Sk = 10^4$ and $KC = 10^{-2}$. The red and blue solid lines correspond to the theoretical estimations of [50], see (16). The dashed lines correspond to the theoretical asymptotic expansion $Sk \to \infty$, see (18). The horizontal dashed lines correspond to the theoretical isolated cylinder limits as $\varepsilon \to \infty$. The symbols correspond to the numerical predictions.

difference might slightly affect the deviation between the theoretical and numerical results. In any case, the relative deviation for $m_{\text{self}}^{(1)}$ (resp. m_{cross}) is smaller than $\iota \leq 0.6\%$ (resp. $\iota \leq 0.2\%$) while the relative deviation for $c_{\text{self}}^{(1)}$ (resp. c_{cross}) is more pronounced, with $\iota \leq 5.5\%$ (resp. $\iota \leq 6.7\%$).

A further analysis is carried out to check the scale invariance of the numerical results obtained for $\varepsilon = 2$, $Sk = 10^4$ and $KC = 10^{-2}$ (see Table A3 in Appendix A). In the numerical simulation, the dimensional quantities were: $D_1 = 1$, $D_2 = 2$, $U = 10^{-2}$ unit of length and $\Omega = 0.0633$ unit of frequency. In this new case study, we set $D_1 = 0.0316$, $D_2 = 0.0632$, $U = 0.0316 \times 10^{-2}$ unit of length and $\Omega = 63.3$ unit of frequency, such that they are self similar configurations in terms of dimensionless numbers: $\varepsilon = 2$, $Sk = 10^4$ and $KC = 10^{-2}$. As expected, the new numerical predictions

Figure 6. Study 1. Evolution of the added coefficients with the Stokes numbers Sk, for $\varepsilon = 2$ and $KC = 10^{-2}$. The solid lines refer to the theoretical estimations of [50], see (16). The dashed lines correspond to the theoretical asymptotic expansion $Sk \to \infty$, see (18). The horizontal dashed lines correspond to the theoretical inviscid limits as $Sk \to \infty$. The symbols correspond to the numerical predictions.

$(m_{\text{self}}^{(1)}, m_{\text{cross}}, c_{\text{self}}^{(1)}, c_{\text{cross}}) = (1.71, -2.71, 0.0496, -0.0510)$ are strictly identical to those obtained for the first case study $(m_{\text{self}}^{(1)}, m_{\text{cross}}, c_{\text{self}}^{(1)}, c_{\text{cross}}) = (1.71, -2.71, 0.0483, -0.0488)$, confirming that the dimensionless added coefficients are functions of Sk, ε and KC.

Finally, we check the symmetry of the fluid added mass and damping matrices for $\varepsilon = 2$, $Sk = 10^4$ and $KC = 10^{-2}$ (see Table A4 in Appendix A). Therefore, the outer cylinder is imposed a sinusoidal displacement in the x-direction for five time periods, i.e. $\mathbf{u}^* = \sin(t^*)\mathbf{e}_x$ with $t^* \in \{0, 10\pi\}$. The numerical predictions for the added coefficients are $(m_{\text{self}}^{(2)}, m_{\text{cross}}, c_{\text{self}}^{(2)}, c_{\text{cross}}) = (6.71, -2.70, 0.0519, -0.0488)$ whereas the theoretical estimations are $(m_{\text{self}}^{(2)}, m_{\text{cross}}, c_{\text{self}}^{(2)}, c_{\text{cross}}) = (6.71, -2.71, 0.0460, -0.0460)$. It follows that the relative deviation between the two approaches is $\iota \le 12.8\%$. We attribute this deviation to the mesh refinement and the larger extension of the surface on which the ALE module acts, compared to the case in which the inner cylinder moves. In fact, in the ALE approach we need to solve an auxiliary Laplace problem, see [45], to compute the mesh velocity, with its own approximations and therefore with an additional numerical error. We shall note that a finer mesh would have reduced this error and normally we would not have observed such differences.
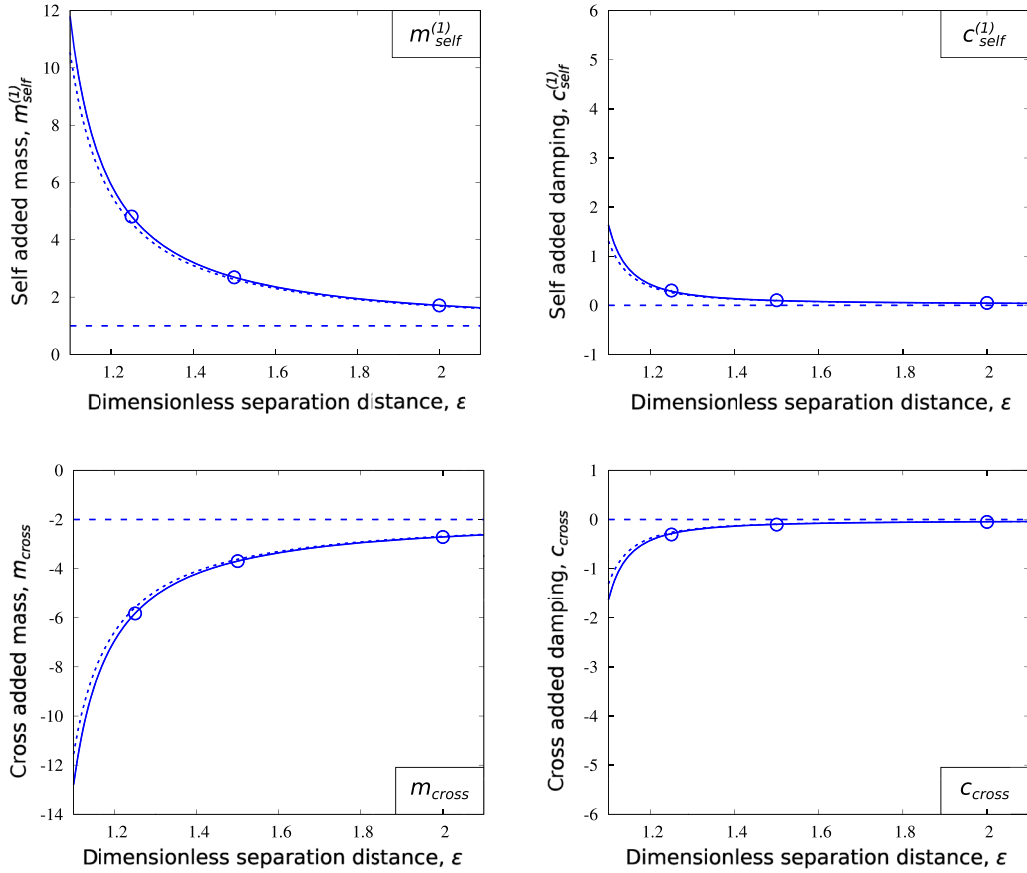
Figure 7. Study 1. Evolution of the added coefficients with the dimensionless separation distances ε, for $Sk = 10^4$ and $KC = 10^{-2}$. The solid lines refer to the theoretical estimations of [50], see (16). The dashed lines correspond to the theoretical asymptotic expansion $Sk \rightarrow \infty$, see (18). The horizontal dashed lines correspond to the theoretical isolated cylinder limits as $\varepsilon \rightarrow \infty$. The symbols correspond to the numerical predictions.

As expected, the numerical simulations confirm that the cross-added coefficients do not depend on which cylinder is moving. Indeed, for $\varepsilon = 2$, $Sk = 10^4$ and $KC = 10^{-2}$, when C_1 moves we obtained $(m_{cross}, c_{cross}) = (-2.71, -0.0488)$ whereas when C_2 moves we have $(m_{cross}, c_{cross}) = (-2.70, -0.0488)$. In other words, the dimensionless fluid force acting on C_1 as C_2 moves is the same as the dimensionless fluid force acting on C_2 as C_1 moves.

As a conclusion to study 1, we show in Figure 9 the pressure distribution in the fluid layer when C_1 is imposed a sinusoidal displacement in the x-direction and C_2 is stationary, for $Sk = 10^4$, $\varepsilon = 2$ and $KC = 10^{-1}$. The numerical and theoretical predictions are in very good agreement as the two snapshots look very similar. Note that these snapshots are taken at a time when C_1 has a positive acceleration. As expected from the inertia effect of the added mass, the fluid pushes C_1 in a direction opposite to its acceleration vector, by creating a negative (resp. positive) pressure on the left (resp. right) side of C_1.

In this section we have thoroughly tested the capabilities of our CFD code in predicting the fluid forces in the case of two coaxial cylinders. In what follows, we challenge the code with a more complicated configuration consisting of a tube bundle immersed in a viscous fluid.
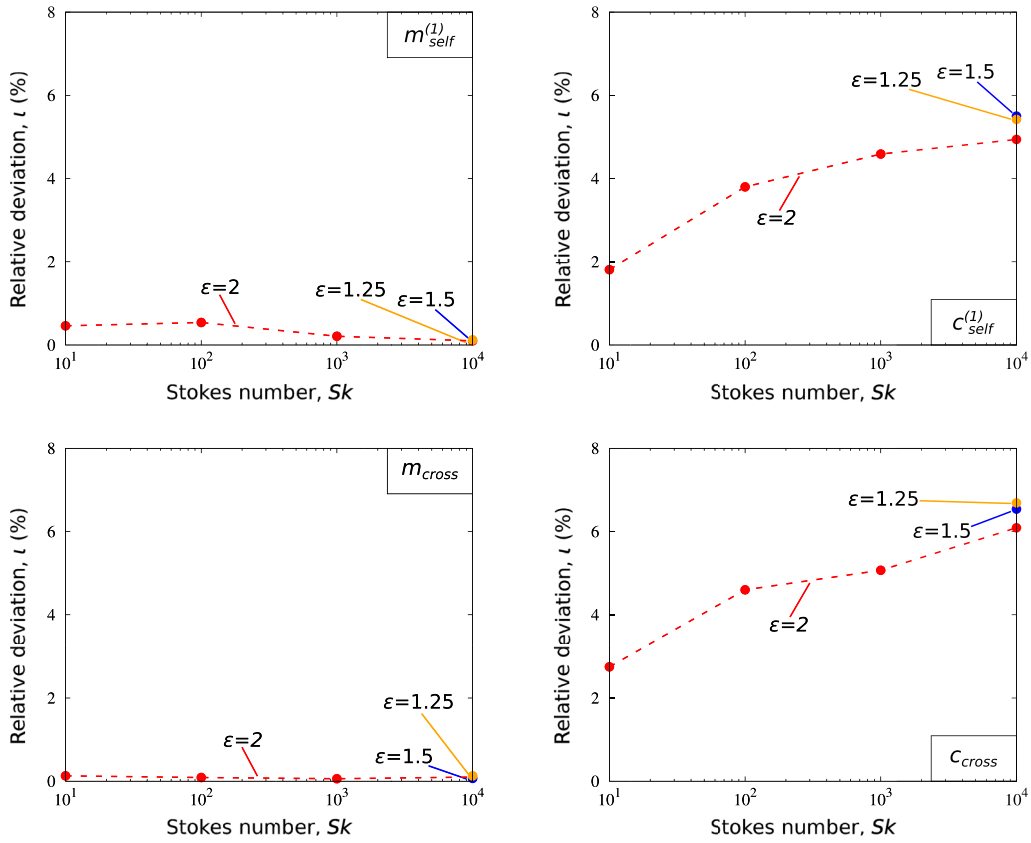
Figure 8. Study 1. Evolution of the relative deviation, ι with the Stokes number, Sk for different values of ε and $KC = 10^{-2}$. The red dotted lines with points refer to $\varepsilon = 2$, the blue points refer to $\varepsilon = 1.5$ while the orange points refer to $\varepsilon = 1.25$.
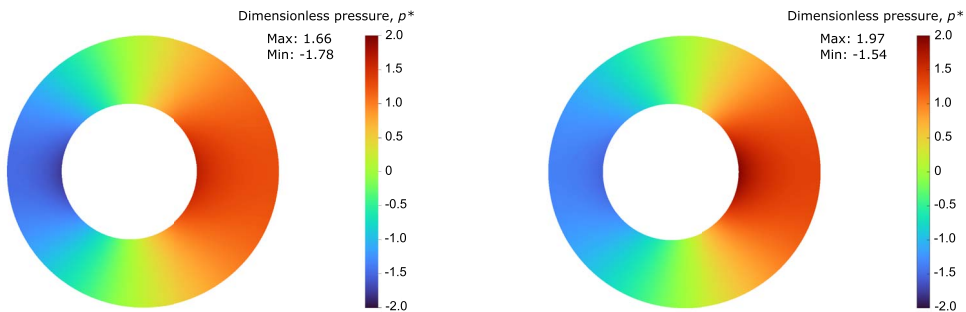
Figure 9. Study 1. Dimensionless pressure field, for $Sk = 10^4$, $\varepsilon = 2$ and $KC = 10^{-1}$. The right side figure corresponds to the theoretical estimation of [49]. The left side figure corresponds to the TrioCFD prediction (the time evolution of the pressure field can be observed in the corresponding movie [52]).
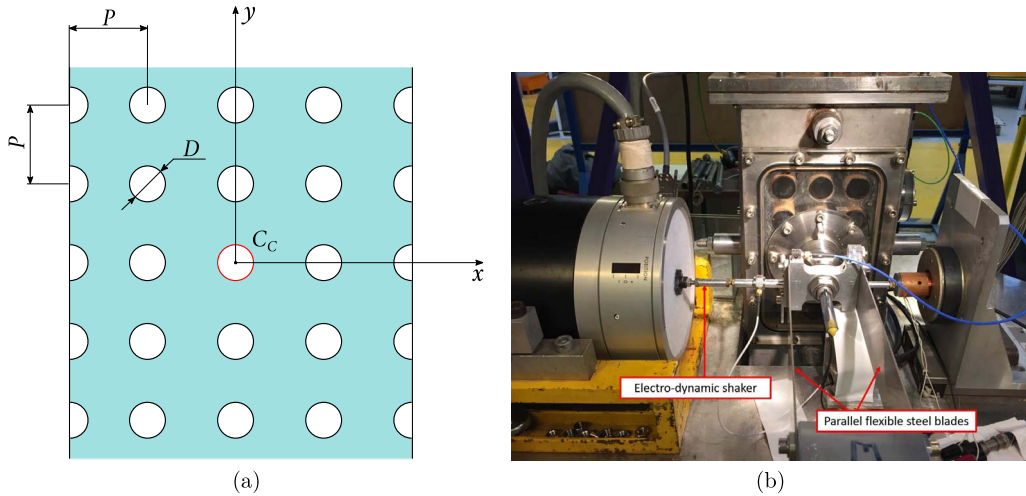
Figure 10. Study 2. (a) Configuration with 3×5 cylinders plus two columns of 5 half-cylinders at the boundaries. The tube bundle is immersed in a homogeneous fluid with mass density ρ and kinematic viscosity ν. (b) Photo of the experimental setup designed to measure the fluid coefficients by the direct method.

4. Study 2. Vibrations of a cylinder in a square tube bundle immersed in a viscous fluid

The importance of fluid-elastic forces in tube bundle vibrations can hardly be over-emphasized, in view of their damaging potential. In the last decades, advanced models for representing the fluid-elastic forces through added-coefficients have therefore been developed by the community of the domain. Those models are nowadays embedded in the methodologies that are used on a regular basis by both steam generators providers and operators, in order to prevent the risk of a tube failure with adequate safety margins. From an R&D point of view however, the need still remains for more advanced models of the fluid added-coefficients, in order to fully decipher the physics underlying the observed phenomena.

In what follows, we aim to determine numerically and experimentally (new measurement setup built at CEA) the effect of the Stokes number Sk on the fluid coefficients, considering the case of a square tube bundle immersed in a viscous fluid at rest. The numerical results obtained with TrioCFD are thoroughly compared with the experimental results and also a theoretical approach proposed by [53].

4.1. *Presentation of the problem*

Let C_C be a cylinder of diameter D, located in the central position of a square tube bundle with pitch P, see Figure 10(a). The cylinder C_C oscillates in the (x, y) plane with a simple harmonic motion of angular frequency Ω and a displacement amplitude U. All the other cylinders are stationary. The tube bundle is immersed in a Newtonian and homogeneous fluid, with mass density ρ and kinematic viscosity ν. The fluid flow generated by the oscillation of the central cylinder is assumed as incompressible and two-dimensional.

Following the approach presented in Section 3 with $D_1 = D_2 = D$, the dimensionless fluid force acting on the central cylinder is expressed as

$$\mathbf{f}^* = -\pi \left(m_{\text{self}} \frac{\mathrm{d}^2 \mathbf{u}^*}{\mathrm{d}t^{*2}} + c_{\text{self}} \frac{\mathrm{d}\mathbf{u}^*}{\mathrm{d}t^*} \right), \tag{22}$$

with m_{self} and c_{self} the self-added mass and damping dimensionless coefficients, respectively. For a given configuration, these coefficients are functions of the pitch ratio P/D, the Keulegan–Carpenter number $KC = U/D$ and the Stokes number $Sk = D^2\Omega/(2\pi/\nu)$.

In order to determine the variations of m_{self} and c_{self} with Sk, an experimental setup consisting of 3×5 cylinders (plus two columns of 5 half-cylinders at the boundaries) has been built at CEA, see Figure 10(b). This setup is briefly presented in the following and the reader is referred to [54–56] for an extensive description. Following the principle of the direct method developed by [57], an electro-dynamic shaker (PRODERA 200 N) is used to impose a harmonic motion to the central tube, supported by two parallel flexible steel blades allowing large vibrations in the x direction. The fluid coefficients are directly extracted from the measure of the fluid force, obtained with two piezo-electric transducers (KISTLER 9132 A). Despite its apparent simplicity, the method of [57] has been progressively abandoned due to its difficulty to implement experimentally. Still, here we reconsider this method, performing some new experiments with a tube bundle with pitch $P = 0.045$ m, made with cylinders of diameter $D = 0.03$ m and length $L = 0.3$ m. The central cylinder is imposed a harmonic displacement in the x-direction with amplitude $U = 0.003$ m and a frequency $F \in \{5, 10, 15, 20, 25\}$ Hz. In terms of dimensionless numbers, this corresponds to a pitch ratio $P/D = 1.5$, a Keulegan–Carpenter number $KC = 10^{-1}$ and a Stokes number $Sk \in \{0.45, 0.90, 1.35, 1.80, 2.25\} \times 10^4$.

In what follows, we aim to compare the experimental results with TrioCFD predictions. In the discussion of our results we also refer to the phenomenological estimations of the fluid coefficients provided by [53] for $KC \ll 1$

$$m_{\text{self}} = \frac{\pi}{4} \frac{(D_e/D)^2 + 1}{(D_e/D)^2 - 1}, \quad c_{\text{self}} = \frac{4}{\sqrt{\pi}} \frac{1}{\sqrt{Sk}} \frac{1 + (D/D_e)^3}{[1 - (D/D_e)^2]^2}, \tag{23}$$

where $D_e = P(1.07 + 0.56 P/D)$ represents an equivalent diameter introduced to model the confinement of the tube bundle.

4.2. *Numerical setup*

The fluid domain is discretized with an unstructured grid of triangles generated by the SALOMÉ platform, see [58].

Before analyzing the meshes used in the numerical simulations and their properties, we start discussing on the technique used to design the geometry. In the experimental setup, the geometry is perfectly symmetrical so that there is no fluid force acting on the cylinders as they are stationary. Numerically, to ensure a zero hydrostatic force, the same discretization scheme of the fluid domain close to every single cylinder is required, while maintaining an x and y symmetry of the mesh grid. To do so, we introduce some artificial lines to subdivide the fluid domain into blocks, each of them being divided into four slices. The automatic and optimized mesh algorithm ensures that the arrangement of the generated triangles, on each side of the artificial lines, is perfectly symmetrical, so that all the slices are discretized equally. The MG-CADSurf Module of SALOMÉ is used for this purpose. We define two mesh sizes: a local size, lc_{fine}, for elements close to the cylinders and a user size, lc for elements far from the cylinders. A gradation parameter is also set, $\Delta = 1.1$, as the maximum ratio between the lengths of two adjacent edges.

First, a mesh sensitivity analysis is carried out on a truncated fluid domain (with the last rows of cylinders cut in half) in order to reduce the time of calculation and speed up the convergence of the grid. This analysis shows that a mesh grid with $lc = 0.0005$ and $lc_{\text{fine}} = 0.00015$ is suitable for an accurate estimation of the fluid forces and the related added coefficients, see Appendix B. Then, the mesh sizes are kept constant whereas the size of the fluid domain is gradually increased by a distance of N_D diameters in the y-directions, with N_D from 1 to 5.
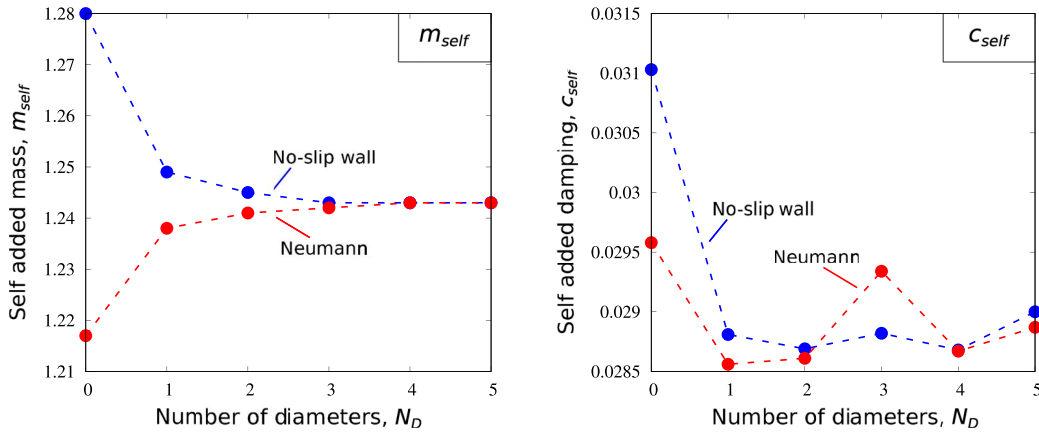
Figure 11. Study 2. Evolution of the self-added coefficients with the size of the fluid domain (the size of the fluid domain increases by a distance of N_D diameters in the y-directions). The blue (resp. red) dashed line corresponds to the numerical predictions obtained with a wall boundary condition (resp. a Neumann boundary condition) imposed on the top and bottom boundaries of the computational domain, see Figure 10. The dimensionless parameters are $Sk = 1.8 \times 10^4$, $P/D = 1.5$ and $KC = 10^{-1}$.

4.3. *Results and discussion*

The central cylinder is allowed to move in the x-direction with a sinusoidal displacement of five time periods, i.e. $\mathbf{u}^* = \sin(t^*)\mathbf{e}_x$ with $t^* \in \{0, 10\pi\}$. The numerical simulations are performed for $Sk \in \{0.45, 0.90, 1.35, 1.80, 2.25\} \times 10^4$ corresponding to imposed frequencies in the range $F \in \{5, 10, 15, 20, 25\}$ Hz. The other parameters are $P/D = 1.5$ and $KC = 10^{-1}$.

Before analyzing the variations of the fluid coefficients, we first discuss the choice of the boundary conditions used in the numerical simulations. In our experiments, the fluid is laterally confined by two parallel plates. Numerically, a classical wall condition ($\mathbf{v} = \mathbf{0}$) is thus applied on the two lateral sides. The choice of the boundary condition at the top and bottom sides of the computational domain (y directions) is more delicate as the tube bundle is experimentally surrounded by two columns of water. To overcome this problem, we determine the size of the computational domain which yields numerical results poorly sensitive to this choice. To do so, we test the effect of two types of y boundary conditions: a wall condition and a Neumann zero stress condition ($p\mathbf{n} - \rho\nu[\nabla\mathbf{v} + (\nabla\mathbf{v})^{\mathrm{T}}] \cdot \mathbf{n} = \mathbf{0}$). In Figure 11, we show the results of this test for $Sk = 1.8 \times 10^4$ as the size of the fluid domain increases by a distance of N_D diameters in the y-directions. As N_D increases, we observe that m_{self} converges to a constant value that does not depend on the choice of the y boundary condition. Similarly, the two types of boundary conditions yield very tiny differences on the values of c_{self}. From these observations, we thus decide to perform all our numerical simulations with $N_D = 4$ and a wall boundary condition in the y-directions.

The time evolution of the dimensionless fluid force is represented in Figure 12. We note that our simulations are in good agreement with both the theoretical and the experimental estimations, despite a small amplitude deviation, in particular with the experimental measurements for $F \in \{5, 20\}$ Hz, i.e. $Sk \in \{0.45, 1.8\} \times 10^4$. This small deviation will be analyzed more precisely in what follows, considering the variations of the fluid coefficients m_{self} and c_{self}.
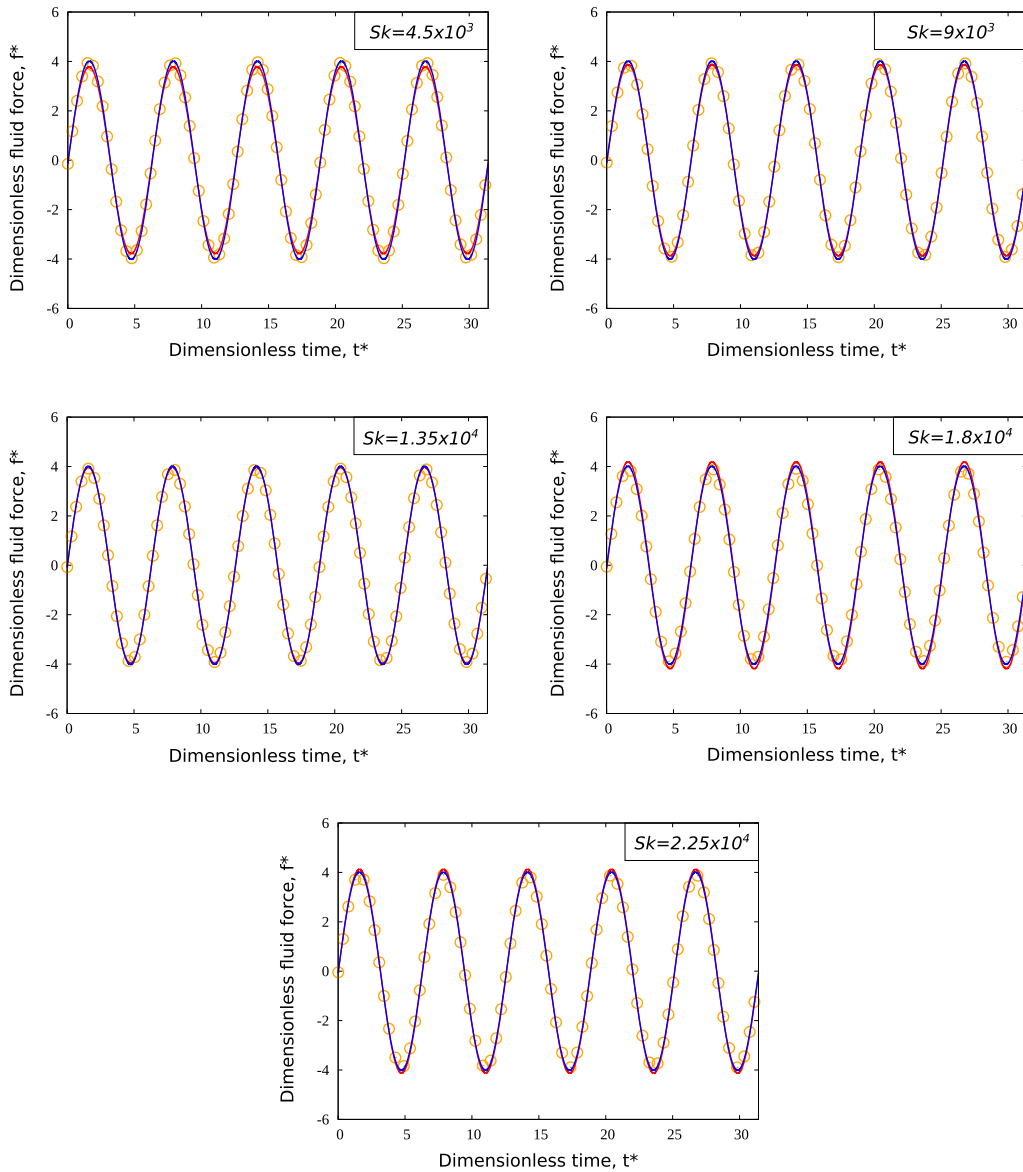
Figure 12. Study 2. Time evolution of the dimensionless fluid forces, for $Sk \in \{0.45, 0.90, 1.35, 1.80, 2.25\} \times 10^4$, $P/D = 1.5$ and $KC = 10^{-1}$. The blue solid lines correspond to the theoretical estimations of [53], see (23). The red solid lines correspond to the experimental measurements. The orange symbols correspond to the numerical predictions. (For interpretation of the colors in this figure, the reader is referred to the web version of this article.)

The evolution of the self-added coefficients with the Stokes number, Sk, is depicted in Figure 13. Our simulations are in good agreement with the theoretical estimations, in the sense that similar trends are recovered, bringing out the same behavior of the fluid coefficients. Still, we note that the simulations tend to underestimate (resp. overestimate) m_{self} (resp. c_{self}), with a
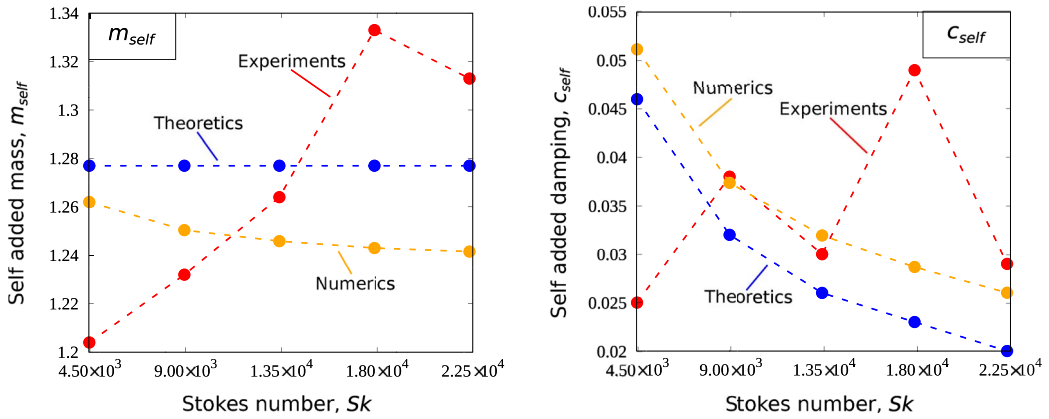
Table 1. Study 2. Table of the self-added coefficients as a function of the Stokes number, Sk and relative deviation, ι

| Sk ($\times 10^4$)	m_{self}		c_{self}	
	ER	AT	ET	AT
	Numerics		Numerics	
	ι^{ER}	ι^{AT}	ι^{ER}	ι^{AT}
	1.20	1.28	0.0250	0.0456
0.45	1.26		0.0512	
	5%	1.6%	104.8%	12.3%
	1.23	1.28	0.0380	0.0323
0.9	1.25		0.0374	
	1.6%	2.3%	1.6%	15.8%
	1.26	1.28	0.0300	0.0263
1.35	1.25		0.0319	
	0.8%	2.3%	6.3%	21.3%
	1.33	1.28	0.0490	0.0228
1.8	1.24		0.0287	
	6.8%	3.1%	41.4%	25.9%
	1.31	1.28	0.0290	0.0204
2.25	1.24		0.0260	
	5.3%	3.1%	10.3%	27.5%

The notations ER and AT refer to the experimental results and the approximate theory. The pitch ratio is $P/D = 1.5$ and the Keulegan–Carpenter number is $KC = 10^{-1}$.

relative deviation always smaller than $\iota \leq 3.1\%$ (resp. $\iota \leq 27.5\%$), see Table 1. We attribute these deviations to the fact that the theoretical approach of [53] is based on a strong approximation in which the tube bundle is modeled as a system of two concentric cylinders, through the definition of a fictive equivalent diameter determined empirically. Also, the theory of [53] relies on a linear approach, contrarily to our numerical simulations in which the nonlinear convective term of the dimensionless Navier–Stokes equation is taken into account. The agreement between the numerical predictions and our experimental results is partial, showing a good agreement for the self-added mass coefficient m_{self}, with $\iota < 7\%$, but some important deviation for c_{self}, especially for the lowest Stokes number $Sk = 0.45 \times 10^4$, where $\iota \approx 105\%$. It shall be noted that it is very delicate to measure the self-damping coefficient in our experiments as the determination of c_{self} relies on a tiny phase difference between the fluid force and the imposed displacement. Also, for such a low Stokes number, i.e. low frequency, our experiments become very sensitive to parasitic frequencies in the experimental setup, leading to a bad signal to noise ratio. Still, these first comparisons are very encouraging and should foster further developments of the experimental direct method.

As a conclusion to study 2, we show in Figure 14 the pressure distribution when C_C is imposed a sinusoidal displacement in the x-direction, for $Sk = 1.8 \times 10^4$, $P/D = 1.5$ and $KC = 10^{-1}$. Note that this snapshot is taken at a time when C_C has a positive acceleration. As expected from the inertia effect of the added mass, the fluid pushes C_C in a direction opposite to its acceleration vector, by creating a negative (resp. positive) pressure on the left (resp. right) side of C_C.

Figure 13. Study 2. Evolution of the self-added coefficients with the Stokes number Sk, for $P/D = 1.5$ and $KC = 10^{-1}$. The red, blue and orange dashed lines with points refer respectively to the experimental measurements, the theoretical estimations of [53] and the numerical predictions.
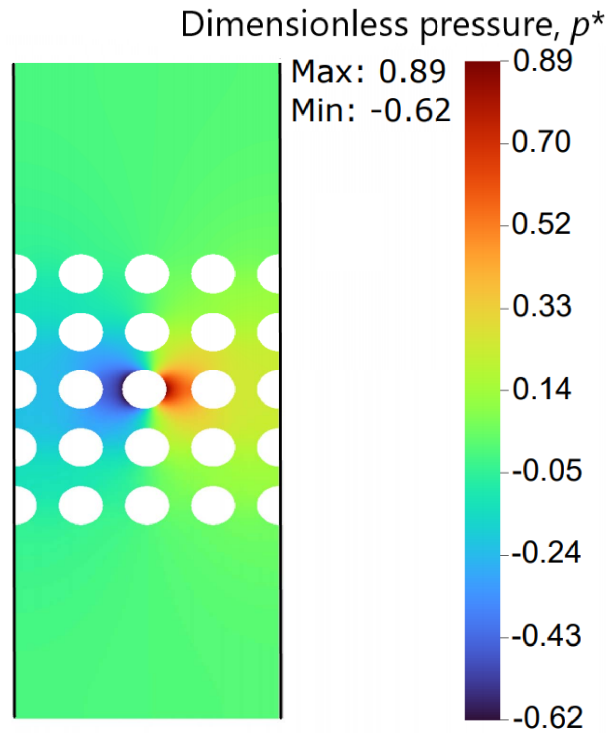
Figure 14. Study 2. Dimensionless pressure field, for $Sk = 1.8 \times 10^{4}$, $P/D = 1.5$ and $KC = 10^{-1}$, computed with TrioCFD.

5. Conclusion and perspectives

In this study, we have first considered the vibration of two coaxial cylinders separated by a viscous fluid. The ALE numerical approach, based on a mesh update technique that considers the motion of the boundary, has been carried out with TrioCFD to estimate the fluid forces acting on the two cylinders.

We started by studying the case in which the outer cylinder is stationary while the inner one is imposed a harmonic motion. The numerical predictions for the fluid forces and the corresponding added coefficients are in very good agreement with the theoretical estimations, even if a tiny difference is observed in the range of low Stokes numbers in which the theoretical estimations reach their limit of validity. More specifically, we have shown that the two forces are in phase opposition and sensitive to the Stokes number, *Sk*, and the dimensionless separation distance, ε. The amplitude (resp. phase) of the forces decreases (resp. increases) as *Sk* or ε increases, recovering the inviscid limit for large Stokes numbers or the limit of an isolated cylinder for large ε. The fluid coefficients variations are also correctly reproduced by the numerical simulations, which are shown to respect the scale invariance expected from the dimensional analysis. We then studied the case in which the inner cylinder is stationary while the outer one is imposed a harmonic motion. From this study, we have shown that the force acting on the stationary cylinder does not depend on which cylinder is moving (inner or outer).

After having successfully tested the capabilities of the ALE method implemented in TrioCFD, in the configuration of two coaxial cylinders, we have considered the problem of a vibrating cylinder located in the central position of a square tube bundle immersed in a viscous fluid. We have shown that the numerical predictions for the self-added mass coefficient are in good agreement with the results of our experiments led at CEA and a theoretical estimation used by engineers. The numerical predictions for the self-added damping coefficient are also in good agreement with the theoretical estimation. They partially agree with the experimental results, showing an important divergence for low Stokes numbers. However, such a deviation is mainly due to our experimental setup, which exhibits a strong sensitivity to parasitic frequencies for low Stokes numbers.

In conclusion, the ALE method implemented in TrioCFD is particularly efficient in solving fluid–structure interaction problems with a fluid initially at rest. We are now confident that further developments will make it possible to tackle three-dimensional problems with an incident fluid flow.

Nomenclature

$\mathbf{v}_{\text{ALE}}$	Velocity of the ALE frame reference
J	Jacobian of the transformation between the ALE and the Lagrange frame reference
Δt	Time step of the numerical simulation
$\mathbf{V}_h, \mathbf{P}_h$	Unknowns vectors of the discrete fluid flow velocity vector and pressure
$[M]$	Mass matrix operator
$[A]$	Discrete diffusion operator
$[L(\mathbf{V}_h)]$	Non-linear discrete convection operator
$[G]$	Discrete gradient operator
$[D]$	Discrete divergence operator
lc, lc_{fine}	Largest and smallest mesh size of the fluid domain
Δ	Maximum ratio between the lengths of two adjacent edges
D_j	Diameter of cylinder C_j
∂C_j	Boundary of cylinder C_j

P	Pitch between the cylinders
Ω	Angular frequency of the cylinders
t, t^*	Dimensional and dimensionless time
∂C_j	Boundary of cylinder C_j
$\mathbf{n}_j$	Outward normal unit vector to cylinder ∂C_j
ρ	Fluid mass density
ν	Fluid kinematic viscosity
$\mathbf{v}, \mathbf{v}^*$	Dimensional and dimensionless fluid flow velocity vector
p, p^*	Dimensional and dimensionless fluid flow pressure
$\mathbf{F}_j, \mathbf{f}_j^*$	Dimensional and dimensionless fluid force on cylinder C_j
h_j, φ_j	Magnitude and phase angle of $\mathbf{f}_j^*$
$\mathbf{U}, \mathbf{u}^*$	Dimensional and dimensionless displacement vector of the cylinders
U	Displacement module of the cylinders
$\mathrm{J}_n, \mathrm{Y}_n$	Bessel functions of the first and second kind
ε	Dimensionless separation distance
KC	Keulegan–Carpenter number
Sk	Stokes number
P/D	Pitch ratio
$\mathbf{e}_x, \mathbf{e}_y$	Cartesian basis vectors
$[M_j], [C_j]$	Added mass and damping matrices
$m_{\mathrm{self}}^{(j)}, c_{\mathrm{self}}^{(j)}$	Self-added mass and damping coefficients
$m_{\mathrm{cross}}, c_{\mathrm{cross}}$	Cross-added mass and damping coefficient
$\widetilde{m}_{\mathrm{self}}^{(j)}, \widetilde{c}_{\mathrm{self}}^{(j)}$	Asymptotic expansion of $m_{\mathrm{self}}^{(j)}$ and $c_{\mathrm{self}}^{(j)}$ as $Sk \to \infty$
$\widetilde{m}_{\mathrm{cross}}, \widetilde{c}_{\mathrm{cross}}$	Asymptotic expansion of m_{cross} and c_{cross} as $Sk \to \infty$
$m_{\mathrm{self}}^{(j)\mathrm{pot}}, c_{\mathrm{self}}^{(j)\mathrm{pot}}$	Inviscid limits of $m_{\mathrm{self}}^{(j)}$ and $c_{\mathrm{self}}^{(j)}$
$m_{\mathrm{cross}}^{\mathrm{pot}}, c_{\mathrm{cross}}^{\mathrm{pot}}$	Inviscid limits of m_{cross} and c_{cross}
ι	Relative deviation between theoretical/experimental and numerical predictions

Declaration of competing interest

The authors declare that they have no known competing financial interests or personal relationships that could have appeared to influence the work reported in this paper.

Acknowledgements

Appendix A. Study 1. Tables of comparison numerics versus theory

In this appendix, we report the tables of comparison between the theoretical and numerical values of the fluid added coefficients for the case study 1, with two coaxial vibrating cylinders. The relative deviation ι is also reported in the tables. The notations ET and AT refer to the exact and asymptotic theories.

Table A1. Study 1. Case 1. Table of the fluid added coefficients as a function of the Stokes number, Sk and relative deviation, ι

Sk	$m_{\text{self}}^{(1)}$		m_{cross}		$c_{\text{self}}^{(1)}$		c_{cross}	
	ET	AT	ET	AT	ET	AT	ET	AT
	Numerics		Numerics		Numerics		Numerics	
	ι^{ET}	ι^{AT}	ι^{ET}	ι^{AT}	ι^{ET}	ι^{AT}	ι^{ET}	ι^{AT}
	2.53	2.30	−3.53	−3.38	2.86	1.43	−2.86	−1.43
10	2.52		−3.54		2.91		−2.94	
	0.4%	5.9%	0.3%	4.7%	1.7%	103.5%	2.8%	105.6%
	2.11	1.89	−3.11	−2.89	0.550	0.451	−0.550	−0.451
10^2	2.10		−3.11		0.570		−0.575	
	0.5%	11.1%	0%	7.6%	3.6%	26.4%	4.5%	27.5%
	1.81	1.74	−2.81	−2.74	0.152	0.143	−0.152	−0.143
10^3	1.81		−2.81		0.159		−0.160	
	0%	4%	0%	2.6%	4.6%	11.2%	5.3%	11.9%
	1.71	1.69	−2.71	−2.69	0.0460	0.0451	−0.0460	−0.0451
10^4	1.71		−2.71		0.0483		−0.0488	
	0%	1.2%	0%	0.7%	5%	7.1%	6.1%	8.2%

The notations ET and AT refer to the exact and asymptotic theories. The numerical values refer to symbols shown in Figure 6. The dimensionless separation distance is $\varepsilon = 2$ and the Keulegan–Carpenter number is $KC = 10^{-2}$.

Table A2. Study 1. Table of the fluid added coefficients as a function of the dimensionless separation distance, ε and relative deviation, ι

ε	$m_{\text{self}}^{(1)}$		m_{cross}		$c_{\text{self}}^{(1)}$		c_{cross}	
	ET	AT	ET	AT	ET	AT	ET	AT
	Numerics		Numerics		Numerics		Numerics	
	ι^{ET}	ι^{AT}	ι^{ET}	ι^{AT}	ι^{ET}	ι^{AT}	ι^{ET}	ι^{AT}
	4.82	4.58	−5.82	−5.58	0.288	0.263	−0.288	−0.263
1.25	4.81		−5.83		0.303		−0.307	
	0.2%	5%	0.2%	4.5%	5.2%	15.2%	6.6%	16.7%
	2.69	2.62	−3.69	−3.62	0.0989	0.0912	−0.0989	−0.0912
1.5	2.69		−3.70		0.104		−0.105	
	0%	2.7%	0.3%	2.2%	5.2%	14%	6.2%	15.1%
	1.71	1.69	−2.71	−2.69	0.0460	0.0451	−0.0460	−0.0451
2	1.71		−2.71		0.0483		−0.0488	
	0%	1.2%	0%	0.7%	5%	7.1%	6.1%	8.2%

The notations ET and AT refer to the exact and asymptotic theories. The numerical values refer to symbols shown in Figure 7. The Stokes number is $Sk = 10^4$ and the Keulegan–Carpenter number is $KC = 10^{-2}$.

Table A3. Study 1. Testing the scale invariance. Table of the fluid added coefficients and the relative deviation, ι

D_1	$m_{\text{self}}^{(1)}$		m_{cross}		$c_{\text{self}}^{(1)}$		c_{cross}	
	ET	AT	ET	AT	ET	AT	ET	AT
	Numerics		Numerics		Numerics		Numerics	
	ι^{ET}	ι^{AT}	ι^{ET}	ι^{AT}	ι^{ET}	ι^{AT}	ι^{ET}	ι^{AT}
	1.71	1.69	−2.71	−2.69	0.0460	0.0451	−0.0460	−0.0451
1	1.71		−2.71		0.0483		−0.0488	
	0%	1.2%	0%	0.7%	5%	7.1%	6.1%	8.2%
	1.71	1.69	−2.71	−2.69	0.0460	0.0451	−0.0460	−0.0451
0.0316	1.71		−2.71		0.0496		−0.0510	
	0%	1.2%	0%	0.7%	7.8%	10%	10.9%	13.1%

The notations ET and AT refer to the exact and asymptotic theories. The Stokes number is $Sk = 10^4$, the dimensionless separation distance is $\varepsilon = 2$ and the Keulegan–Carpenter number is $KC = 10^{-2}$.

Table A4. Study 1. Testing the symmetry of the fluid added mass and damping matrices. Table of the fluid added coefficients and the relative deviation, ι

	$m_{\text{self}}^{(j)}$		m_{cross}		$c_{\text{self}}^{(j)}$		c_{cross}	
	ET	AT	ET	AT	ET	AT	ET	AT
	Numerics		Numerics		Numerics		Numerics	
	ι^{ET}	ι^{AT}	ι^{ET}	ι^{AT}	ι^{ET}	ι^{AT}	ι^{ET}	ι^{AT}
	1.71	1.69	−2.71	−2.69	0.0460	0.0451	−0.0460	−0.0451
$j = 1$	1.71		−2.71		0.0483		−0.0488	
	0%	1.2%	0%	0.7%	5%	7.1%	6.1%	8.2%
	6.71	6.69	−2.71	−2.69	0.0460	0.0451	−0.0460	−0.0451
$j = 2$	6.71		−2.70		0.0519		−0.0488	
	0%	0.3%	0.4%	0.4%	12.8%	15.1%	6.1%	8.2%

The notations ET and AT refer to the exact and asymptotic theories. The Stokes number is $Sk = 10^4$, the dimensionless separation distance is $\varepsilon = 2$ and the Keulegan–Carpenter number is $KC = 10^{-2}$.

Appendix B. Effect of the mesh size and time step on the fluid added coefficients

In this appendix, we report the mesh converge analysis performed for both cases study. For the case study 1, in Tables B1–B5 we clearly show a convergence of the mass coefficients as lc and lc_{fine} are changed. The convergence of the damping coefficients is less obvious, especially for high values of Sk. Physically, this is related to the thickness of the boundary layer, which tends to zero as Sk increases. It follows that a finer mesh is required close to a cylinder boundary to account for the thickness of the boundary layer and obtain an accurate estimation of the damping terms. Moreover, all the simulations are performed with $CFL = 1$ to ensure maximum precision, except for the simulations with a low value of the Stokes number, $Sk \in \{10^1, 10^2\}$ and $\varepsilon = 2$ where the CFL is progressively increased from 1 to 10, without influencing the quality of the results. Following the numerical approach of the case study 1, we perform a mesh sensitivity analysis on the case study 2, see Table B6.

Table B1. Study 1. Effect of the mesh size on the fluid added coefficients

Sk	lc	lc_{fine}	CFL	$m_{\text{self}}^{(1)}$	m_{cross}	$c_{\text{self}}^{(1)}$	c_{cross}
10^4	0.020	0.005	1	4.83	−5.87	0.320	−0.338
	0.015	0.003	1	4.81	−5.83	0.303	−0.307

The dimensionless separation distance is $\varepsilon = 1.25$ and the Keulegan–Carpenter number is $KC = 10^{-2}$.

Table B2. Study 1. Effect of the mesh size on the fluid added coefficients

Sk	lc	lc_{fine}	CFL	$m_{\text{self}}^{(1)}$	m_{cross}	$c_{\text{self}}^{(1)}$	c_{cross}
10^4	0.015	0.003	1	2.69	−3.70	0.106	−0.108
	0.010	0.002	1	2.69	−3.70	0.104	−0.105

The dimensionless separation distance is $\varepsilon = 1.5$ and the Keulegan–Carpenter number is $KC = 10^{-2}$.

Table B3. Study 1. Effect of the mesh size on the fluid added coefficients

Sk	lc	lc_{fine}	CFL	$m_{\text{self}}^{(1)}$	m_{cross}	$c_{\text{self}}^{(1)}$	c_{cross}
10^1	0.040	0.010	1–100	2.51	−3.55	2.92	−2.97
	0.020	0.005	1–10	2.52	−3.54	2.91	−2.94
10^2	0.040	0.010	1	2.09	−3.12	0.570	−0.579
	0.020	0.005	1–10	2.10	−3.11	0.570	−0.575
10^3	0.040	0.010	1	1.80	−2.82	0.164	−0.170
	0.020	0.005	1	1.80	−2.81	0.160	−0.162
	0.015	0.003	1	1.80	−2.81	0.159	−0.161
	0.010	0.002	1	1.81	−2.81	0.159	−0.160
10^4	0.040	0.010	1	1.70	−2.73	0.0838	−0.110
	0.020	0.005	1	1.71	−2.72	0.0580	−0.0656
	0.015	0.003	1	1.71	−2.72	0.0517	−0.0548
	0.010	0.002	1	1.71	−2.71	0.0495	−0.0509
	0.010	0.001	1	1.71	−2.71	0.0483	−0.0488

The dimensionless separation distance is $\varepsilon = 2$ and the Keulegan–Carpenter number is $KC = 10^{-2}$.

Table B4. Study 1. Testing the scale invariance. Effect of the mesh size on the fluid added coefficients

Sk	lc	lc_{fine}	CFL	$m_{\text{self}}^{(1)}$	m_{cross}	$c_{\text{self}}^{(1)}$	c_{cross}
10^4	0.00050	0.00010	1	1.71	−2.72	0.0528	−0.0567
	0.00032	0.00006	1	1.71	−2.71	0.0496	−0.0510

The dimensionless separation distance is $\varepsilon = 2$ and the Keulegan–Carpenter number is $KC = 10^{-2}$.

Table B5. Study 1. Testing the symmetry of the fluid added mass and damping matrices. Effect of the mesh size on the fluid added coefficients

Sk	lc	lc_{fine}	CFL	$m_{\text{self}}^{(2)}$	m_{cross}	$c_{\text{self}}^{(2)}$	c_{cross}
	0.0100	0.0030	1	6.71	−2.70	0.0667	−0.0534
10^4	0.0100	0.0020	1	6.71	−2.70	0.0554	−0.0488
	0.0075	0.0015	1	6.71	−2.70	0.0519	−0.0488

The dimensionless separation distance is $\varepsilon = 2$ and the Keulegan–Carpenter number is $KC = 10^{-2}$.

Table B6. Study 2. Effect of the mesh size on the fluid added coefficients

$Sk(\times 10^4)$	lc	lc_{fine}	Δ	CFL	m_{self}	c_{self}
	0.0008	0.00030	1.1	1	1.30	0.0547
0.45	0.0005	0.00015	1.1	1	1.30	0.0535
	0.0004	0.00010	1.1	1	1.30	0.0537

The pitch ratio is $P/D = 1.5$ and the Keulegan–Carpenter number is $KC = 10^{-1}$.

References

[1] S. B. Furber, J. E. Ffowcs Williams, "Is the Weis–Fogh principle exploitable in turbomachinery?", *J. Fluid Mech.* **94** (1979), p. 519-540.

[2] S. S. Chen, "Dynamics of heat exchanger tube banks", *J. Fluids Eng.* **99** (1977), p. 462-469.

[3] R. Lagrange, P. Piteau, X. Delaune, J. Antunes, "Fluid-elastic coefficients in single phase cross flow: Dimensional analysis, direct and indirect experimental methods", in *Pressure Vessels and Piping Conference*, Fluid–Structure Interaction, vol. 4, ASME, New York, NY, 2019, p. 93984.

[4] K. Singh, S. Michelin, E. De Langre, "Energy harvesting from axial fluid-elastic instabilities of a cylinder", *J. Fluids Struct.* **30** (2012), p. 159-172.

[5] S. Michelin, O. Doare, "Energy harvesting efficiency of piezoelectric flags in axial flows", *J. Fluid Mech.* **714** (2013), p. 489-504.

[6] E. Virot, X. Amandolese, P. Hemon, "Coupling between a flag and a spring-mass oscillator", *J. Fluids Struct.* **65** (2016), p. 447-454.

[7] C. Eloy, R. Lagrange, C. Souilliez, L. Schouveiler, "Aeroelastic instability of cantilevered flexible plates in uniform flow", *J. Fluid Mech.* **611** (2008), p. 97-106.

[8] G. G. Stokes, "On the effect of the internal friction of fluids on pendulums", *Trans. Camb. Phil. Soc.* **9** (1851), p. 8-106.

[9] G. H. Keulegan, L. H. Carpenter, "Forces on cylinders and plates in an oscillating fluid", *J. Res. Natl. Bur. Stand.* **60** (1958), article no. 2857.

[10] C. J. Garrison, R. B. Berklitc, "Hydrodynamic loads induced by earthquakes", in *Offshore Technology Conference*, vol. 1, OnePetro, Richardson, TX, 1972, p. 429-442.

[11] T. Sarpkaya, "Separated flow about lifting bodies and impulsive flow about cylinders", *Am. Inst. Aeronaut. Astronaut. J.* **4** (1966), p. 414-420.

[12] A. R. Chandrasekaran, S. S. Saini, "Vibration of submerged structures", *Water Energy Int.* **28** (1971), p. 263-268.

[13] R. A. Skop, S. E. Ramberg, K. M. Ferer, in *Added Mass and Damping Forces on Circular Cylinders*, Dept. of Defense, Dept. of the Navy, Office of Naval Research, Naval Research Laboratory; Springfield, Washington, 1976.

[14] T. Sarpkaya, "Forces on cylinders and spheres in a sinusoidally oscillating fluid", *J. Appl. Mech.* **42** (1975), p. 32-37.

[15] L. H. Carpenter, "On the motion of two cylinders in an ideal fluid", *J. Res. Natl. Bur. Stand.* **61** (1958), p. 83-87.

[16] L. Landweber, A. Shahshahan, "Added masses and forces on two bodies approaching central impact in an inviscid fluid", Tech. Report 346, Iowa Institute of Hydraulic Research, Iowa City, IA, 1991.

[17] W. M. Hicks, "On the motion of two cylinders in a fluid", *Q. J. Pure Appl. Math.* **16** (1879), p. 113-140, 193–219.

[18] A. G. Greenhill, "Functional images in cartesians", *Q. J. Pure Appl. Math.* **18** (1882), no. 182, p. 356-362.

[19] G. Birkhoff, *Hydrodynamics*, 2nd ed., Princeton University Press, Princeton, New Jersey, 1960.

[20] R. J. Gibert, M. Sagner, "Vibration of structures in a static fluid medium", *La Houille Blanche* **1/2** (1980), p. 204-262.

[21] D. A. Burton, J. Gratus, R. W. Tucker, "Hydrodynamic forces on two moving discs", *Theor. Appl. Mech.* **31** (2004), p. 153-188.

[22] A. A. Tchieu, D. Crowdy, A. Leonard, "Fluid–structure interaction of two bodies in an inviscid fluid", *Phys. Fluids* **22** (2010), article no. 107101.

[23] Y. M. Scolan, S. Etienne, "On the use of conformal mapping for the computation of hydrodynamic forces acting on bodies of arbitrary shape in viscous flow. Part 2: multi-body configuration", *J. Eng. Math.* **61** (2008), p. 17-34.

[24] D. G. Crowdy, "Analytical solutions for uniform potential flow past multiple cylinders", *Eur. J. Mech. (B/Fluids)* **25** (2006), p. 459-470.

[25] D. G. Crowdy, "A new calculus for two-dimensional vortex dynamics", *Theor. Comput. Fluid Dyn.* **24** (2010), p. 9-24.

[26] R. Lagrange, X. Delaune, P. Piteau, L. Borsoi, J. Antunes, "A new analytical approach for modeling the added mass and hydrodynamic interaction of two cylinders subjected to large motions in a potential stagnant fluid", *J. Fluids Struct.* **77** (2018), p. 102-114.

[27] R. Lagrange, Y. Fraigneau, "New estimations of the added mass and damping of two cylinders vibrating in a viscous fluid, from theoretical and numerical approaches", *J. Fluids Struct.* **92** (2020), article no. 102818.

[28] R. Lagrange, M. A. Puscas, "Hydrodynamic interaction between two flexible finite length coaxial cylinders: New theoretical formulation and numerical validation", *J. Appl. Mech.* **89** (2022), no. 8, article no. 081006.

[29] A. Gronski, G. Artana, "A simple and efficient direct forcing immersed boundary method combined with a high order compact scheme for simulating flows with moving rigid boundaries", *Comput. Fluids* **124** (2016), p. 86-104.

[30] Y. Cheny, O. Botella, "Ls-stag method: A new immersed boundary/level-set method for the computation of incompressible viscous flows in complex moving geometries with good conservation properties", *J. Comput. Phys.* **229** (2010), p. 1043-1076.

[31] R. Mittal, G. Iaccarino, "Immersed boundary methods", *Annu. Rev. Fluid Mech.* **37** (2005), p. 239-261.

[32] B. Kadoch, D. Kolomenskiy, P. Angot, K. Schneider, "A volume penalization method for incompressible flows and scalar advection diffusion with moving obstacles", *J. Comput. Phys.* **231** (2012), p. 4365-4383.

[33] K. Schneider, "Immersed boundary methods for numerical simulation of confined fluid and plasma turbulence in complex geometries: a review", *J. Plasma Phys.* **81** (2015), article no. 435810601.

[34] M. Minguez, R. Pasquetti, E. Serre, "High-order large-eddy simulation of flow over the Ahmed body car model", *Phys. Fluids* **20** (2008), article no. 095101.

[35] C. Nore, D. Castanon Quiroz, L. Cappanera, J. L. Guermond, "Numerical simulation of the von Karman sodium dynamo experiment", *J. Fluid Mech.* **854** (2018), p. 164-195.

[36] J. Donea, A. Huerta, J. P. Ponthot, A. Rodríguez-Ferran, *Arbitrary Lagrangian–Eulerian Methods*, American Cancer Society, Atlanta, GA, 2004.

[37] G. Fourestey, S. Piperno, "A second-order time-accurate ALE Lagrange–Galerkin method applied to wind engineering and control of bridge profiles", *Comput. Meth. Appl. Mech. Eng.* **193** (2004), p. 4117-4137.

[38] B. Koobus, C. Farhat, H. Tran, "Computation of unsteady viscous flows around moving bodies using the k–ε turbulence model on unstructured dynamic grids", *Comput. Meth. Appl. Mech. Eng.* **190** (2000), p. 1441-1466.

[39] P. E. Angeli, U. Bieder, G. Fauchet, "Overview of the TrioCFD code: Main features, V&V procedures and typical applications to nuclear engineering", in *Proceedings of 16th International Topical Meeting on Nuclear Reactor Thermal Hydraulics (NURETH-16), Chicago, USA*, American Nuclear Society, La Grange Park, IL, 2015, p. 252.

[40] P. E. Angeli, M. A. Puscas, G. Fauchet, A. Cartalade, "FVCA8 benchmark for the Stokes and Navier–Stokes equations with the TrioCFD code—benchmark session", in *Finite Volumes for Complex Applications VIII—Methods and Theoretical Aspects*, Springer, Cham, 2017, p. 181-202.

[41] C. Fiorini, B. Després, M. A. Puscas, "Sensitivity equation method for the Navier–Stokes equations applied to uncertainty propagation", *Int. J. Numer. Meth. Fluids* **93** (2020), no. 1, p. 71-92.

[42] M. A. Puscas, L. Monasse, "A three-dimensional conservative coupling method between an inviscid compressible flow and a moving rigid solid", *SIAM J. Sci. Comput.* **37** (2015), p. B884-B909.

[43] M. A. Puscas, L. Monasse, A. Ern, C. Tenaud, C. Mariotti, V. Daru, "A time semi-implicit scheme for the energy-balanced coupling of a shocked fluid flow with a deformable structure", *J. Comput. Phys.* **296** (2015), p. 241-262.

[44] M. A. Puscas, L. Monasse, A. Ern, C. Tenaud, C. Mariotti, "A conservative embedded boundary method for an inviscid compressible flow coupled with a fragmenting structure", *Int. J. Numer. Meth. Eng.* **103** (2015), p. 970-995.

[45] F. Duarte, R. Gormaz, S. Natesan, "Arbitrary Lagrangian–Eulerian method for Navier–Stokes equations with moving boundaries", *Comput. Meth. Appl. Mech. Eng.* **193** (2004), p. 4819-4836.

[46] A. J. Chorin, "Numerical solution of the Navier–Stokes equations", *Math. Comput.* **22** (1968), p. 745-762.

[47] R. Temam, "Une méthode d'approximation de la solution des équations de Navier–Stokes", *Bull. Soc. Math. Fr.* **96** (1968), p. 115-152.

[48] Y. Saad, M. H. Schultz, "GMRES: A generalized minimal residual algorithm for solving nonsymmetric linear systems", *SIAM J. Sci. Statist. Comput.* **7** (1986), no. 3, p. 856-869.

[49] S. S. Chen, M. W. Wambsganss, J. A. Jendrzejczyk, "Added mass and damping of a vibrating rod in confined viscous fluids", *J. Appl. Mech.* **43** (1976), p. 325-329.

[50] T. T. Yeh, S. S. Chen, "The effect of fluid viscosity on coupled tube/fluid vibrations", *J. Sound Vib.* **59** (1978), no. 3, p. 453-467.

[51] C. Geuzaine, J.-F. Remacle, "Gmsh: a three-dimensional finite element mesh generator with built-in pre- and post-processing facilities", *Int. J. Numer. Meth. Eng.* **79** (2009), p. 1309-1331.

[52] R. Lagrange, "Hydrodynamic interaction of two coaxial cylinders", https://www.youtube.com/watch?v=7FxlJeH11jQ&feature=emb_logo&ab_channel=RomainLagrange.

[53] M. J. Pettigrew, C. E. Taylor, N. Subash, "Flow-induced vibration specifications for steam generators and liquid heat exchangers", Tech. report, Atomic Energy of Canada Ltd., Ontario, 1995.

[54] S. Caillaud, E. de Langre, P. Piteau, "The measurement of fluidelastic effects at low reduced velocities using piezo-electric actuators", *ASME J. Press. Vessel Technol.* **121** (1999), p. 232-238.

[55] S. Caillaud, E. de Langre, F. Baj, "Active vibration control for the measurement of fluidelastic effects", *ASME J. Press. Vessel Technol.* **125** (2003), no. 2, p. 165-170.

[56] P. Piteau, X. Delaune, J. Antunes, L. Borsoi, "Experiments and computations of a loosely supported tube in a rigid bundle subjected to single-phase flow", *J. Fluids Struct.* **28** (2012), p. 56-71.

[57] H. Tanaka, S. Takahara, "Fluidelastic vibration of tube arrays in cross-flow", *J. Sound Vib.* **77** (1981), p. 19-37.

[58] A. Ribes, C. Caremoli, "Salomé platform component model for numerical simulation", in *31st Annual International Computer Software and Applications Conference (COMPSAC 2007)*, vol. 2, IEEE, Piscataway, NJ, 2007, p. 553-564.